1 **Title page**

2

3 # Hyperphosphatemia increases inflammation to exacerbate anemia and skeletal muscle
4 # wasting independently of FGF23-FGFR4 signaling

5

6 **Authors and Affiliations:**

7 Brian Czaya, Ph.D.[1], Kylie Heitman, B.Sc.[1], Isaac Campos, B.Sc.[1], Christopher Yanucil, Ph.D.[1],
8 Dominik Kentrup, Ph.D.[1], David Westbrook, M.S.[1], Orlando Gutierrez, M.D.[1], Jodie L. Babitt,
9 M.D.[2], Grace Jung, B.Sc.[3], Isidro B. Salusky, M.D.[4], Mark R. Hanudel, M.D.[4] and Christian
10 Faul, Ph.D.[1*]

11

12 [1]Division of Nephrology and Hypertension, Department of Medicine, The University of
13 Alabama at Birmingham, Birmingham, AL, USA

14 [2]Division of Nephrology, Program in Membrane Biology, Massachusetts General Hospital,
15 Harvard Medical School, Boston, MA, USA

16 [3]Center for Iron Disorders, David Geffen School of Medicine at UCLA, Los Angeles, CA, USA

17 [4]Department of Pediatrics, David Geffen School of Medicine at UCLA, Los Angeles, CA, USA

18

***Contact Information:**

Christian Faul, Ph.D.

Tinsley Harrison Tower 611L

1720 2nd Avenue South

Birmingham, AL, 35205, USA

Telephone: 205-996-9641

Fax: 205-996-6650

Email: cfaul@uabmc.edu

Running headline

Hyperphosphatemia contributes to inflammation, anemia and muscle wasting

Word count (including text of legends and references): 15,115

Abstract

Elevations in plasma phosphate concentrations (hyperphosphatemia) occur in chronic kidney disease (CKD), in certain genetic disorders, and following the intake of a phosphate-rich diet. Whether hyperphosphatemia and/or associated changes in metabolic regulators, including elevations of fibroblast growth factor 23 (FGF23) directly contribute to specific complications of CKD is uncertain. Here we report that similar to patients with CKD, mice with adenine-induced CKD develop inflammation, anemia and skeletal muscle wasting. These complications are also observed in mice fed high phosphate diet even without CKD. Ablation of pathologic FGF23-FGFR4 signaling did not protect mice on an increased phosphate diet or mice with adenine-induced CKD from these sequelae. However, low phosphate diet ameliorated anemia and skeletal muscle wasting in a genetic mouse model of CKD. Our mechanistic *in vitro* studies indicate that phosphate elevations induce inflammatory signaling and increase hepcidin expression in hepatocytes, a potential causative link between hyperphosphatemia, anemia and skeletal muscle dysfunction. Our study suggests that high phosphate intake, as caused by the consumption of processed food, may have harmful effects irrespective of pre-existing kidney injury, supporting not only the clinical utility of treating hyperphosphatemia in CKD patients but also arguing for limiting phosphate intake in healthy individuals.

Introduction

Phosphate (Pi) is an essential mineral nutrient (Erem and Razzaque, 2018). Once absorbed and in circulation, Pi is utilized by cells for various structures and functions. Pi metabolism is regulated by a specific set of hormones to maintain physiological Pi concentrations. Fibroblast growth factor 23 (FGF23) is the chief hormone maintaining body Pi balance by promoting renal Pi excretion when Pi load is high (Fukumoto and Yamashita, 2007; Isakova et al., 2011). Dysregulation of this system causes either low (hypophosphatemia) or high (hyperphosphatemia) serum Pi levels (Farrow et al., 2011; White et al., 2001; Wolf, 2012). Hyperphosphatemic states can result from various conditions, including rare genetic disorders, such as familial tumoral calcinosis (FTC), and acquired diseases, such as chronic kidney disease (CKD), which are more frequent. Moreover, increased consumption of foods and drinks rich in Pi-based additives is expanding in Westernized diets, leading to excess dietary Pi intake (Carrigan et al., 2014; Gutiérrez et al., 2010).

CKD patients have an increased risk of death that is attributable to complications such as inflammation, anemia and skeletal muscle wasting (Amdur et al., 2016; Hoshino et al., 2020; Stenvinkel et al., 2016). The etiology of CKD-associated anemia is multifactorial and includes absolute iron deficiency and functional iron deficiency, with the latter caused by inflammatory cytokines including interleukin-6 (IL6) and interleukin-1β (IL1β). These inflammatory mediators can directly induce the release of the liver-hormone hepcidin, the master regulator of iron metabolism (Falzacappa et al., 2007; Ganz and Nemeth, 2012; Kanamori et al., 2017). Hepcidin controls the flow of iron into circulation by regulating the iron exporter ferroportin (FPN) (Nemeth et al., 2004b). Hepcidin binding occludes FPN (Aschemeyer et al., 2018; Billesbølle et al., 2020) and induces its degradation, thereby restricting iron efflux into the circulation from

iron recycling macrophages, a process also known as reticuloendothelial system (RES) blockade, and from duodenal enterocytes responsible for dietary iron absorption. Collectively, these events reduce serum iron levels (hypoferremia), limiting the supply of iron for erythrocyte production (Nemeth et al., 2004a).

Inflammatory cytokines such as IL6 and IL1β also act on skeletal muscle and induce muscle wasting, a comorbidity affecting 65% of CKD patients (Kovesdy et al., 2013; Li et al., 2009; Zhang et al., 2013). The loss of protein from muscle is ascribed to protein degradation by the ubiquitin-proteasome system, suppression of protein synthesis and impaired growth of new muscle fibers (Wang and Mitch, 2014). As pleotropic activities of IL6 and IL1β induce the production of myostatin, a pivotal mediator of skeletal muscle wasting, these actions foster the simultaneous induction of atrophy-related gene programs and reduced cellular responses to pro-growth signals, which initiates protein synthesis suppression. Together, inflammation and myostatin advance these CKD-associated comorbidities which reduce the survival and quality of life of CKD patients (Zhang et al., 2011).

A prominent aspect of CKD is altered mineral metabolism, where hyperphosphatemia and excess serum FGF23 are factors associated with inflammation, anemia and mortality (Mehta et al., 2017; Mendoza et al., 2017; Navarro-González et al., 2009; Tran et al., 2016). Drugs have been developed to control hyperphosphatemia, but reports show conflicting results about outcomes. Studies of the effects of dietary Pi restriction in animal models are scarce. Dietary interventions to lower phosphate intake are challenging because they require long-term behavioral changes made more difficult by the lack of disclosure of Pi content of foods and beverages by the food industry (Gutiérrez and Wolf, 2010).

All cell types rely on Pi for housekeeping roles, and metabolic Pi uptake is facilitated by three families of sodium-Pi (Na/Pi) cotransporters. Type III Na/Pi cotransporters, PiT-1 and PiT-2, are ubiquitously expressed and mediate cellular Pi homeostasis in all cells (Lederer and Miyamoto, 2012). Pathologic Pi accumulation in vasculature is mediated by PiT-1 and PiT-2, loading Pi into vascular smooth muscle cells where it activates signaling networks such as Ras/mitogen-activated protein kinase (MAPK) and nuclear factor kappa-light-chain-enhancer of activated B cells (NFκB) (Chavkin et al., 2015; Turner et al., 2020; Zhao et al., 2011). These pathways provide plausible pathomechanisms that support excess Pi as a potential culprit behind the clinical association between hyperphosphatemia and CKD-associated vascular calcification.

Under physiologic conditions, bone-derived FGF23 targets the kidney to increase Pi excretion by activating its canonical signaling complex, fibroblast growth factor receptor 1 (FGFR1) and co-receptor Klotho (Czaya and Faul, 2019a). When FGF23 is in pathological excess, as found in dietary Pi overload or CKD, increased FGF23 targets the heart and liver by activating FGFR4, independently of Klotho (Faul et al., 2011; Grabner et al., 2015; Singh et al., 2016). This non-canonical mechanism recruits FGFR4 as a pathologic receptor mediating the effects of excess FGF23 to cause cardiac hypertrophy and promote inflammation (Faul et al., 2011; Grabner et al., 2015; Han et al., 2020; Leifheit-Nestler et al., 2017; Singh et al., 2016; Xiao et al., 2019). However, whether excess FGF23 and/or Pi directly contribute to functional iron deficiency or skeletal muscle wasting is unknown, and direct actions of excess Pi on the liver have not been studied to date.

In this study, we examine whether hyperphosphatemia and/or pathologic FGF23-FGFR4 signaling aggravates functional iron deficiency and skeletal muscle wasting, the common comorbidities in CKD. We expose mice constitutively lacking FGFR4 to hyperphosphatemia in

the absence and presence of CKD. To further define the contribution of hyperphosphatemia, we subject Alport mice, a genetic model of progressive CKD, to a low Pi diet treatment. We identify a molecular mechanism in cultured mouse primary hepatocytes that links excess Pi to its actions on inflammation and iron metabolism, as increased inflammatory cytokines promote widespread pathologies and hepcidin production. Our findings reveal additional complications of hyperphosphatemia besides vascular calcification and identify plausible pathomechanisms underlying clinical associations between inflammation, anemia and skeletal muscle wasting, which could be targeted therapeutically.

Results

FGF23-FGFR4 signaling does not contribute to functional iron deficiency in adenine-induced CKD

To examine FGF23 inflammatory actions *in vivo*, we explored pathologic FGF23-FGFR4 signaling and its role in functional iron deficiency. We subjected wild-type ($FGFR4^{+/+}$) and constitutive FGFR4 knockout ($FGFR4^{-/-}$) mice to adenine diet to induce CKD. Following adenine diet for 14 weeks, $FGFR4^{+/+}$ and $FGFR4^{-/-}$ mice display comparable renal dysfunction, as shown by elevations in blood urea nitrogen (BUN) and serum creatinine levels (Fig. 1a). On adenine diet, serum FGF23 and Pi levels significantly increased in both genotypes (Fig. 1b), as expected with marked kidney injury. No significant changes in serum calcium levels were observed between genotypes on adenine (Supplemental Fig. 1a), despite increased serum Pi levels (Fig. 1b).

We assessed gene expression of inflammatory cytokines and acute phase proteins in both genotypes in adenine-induced CKD. Unlike in healthy control mice, liver IL1β (*Il1b*), IL6 (*Il6*) and serum amyloid A1 (*Saa1*) transcript levels were significantly and similarly elevated (Fig. 1c, d) in both *FGFR4*$^{+/+}$ and *FGFR4*$^{-/-}$ mice.

To identify if FGF23-FGFR4 signaling contributes to functional iron deficiency, we evaluated liver hepcidin (*Hamp*) mRNA and hematological responses. Compared with control mice, *Hamp* transcript levels were significantly and similarly elevated in both *FGFR4*$^{+/+}$ and *FGFR4*$^{-/-}$ mice on adenine (Fig. 1e). Complete blood count and serum analyses displayed significant reductions in red blood cell (RBC) count, mean corpuscular volume (MCV), hemoglobin and serum iron levels on adenine diet (Fig. 1f). Significant reductions in hematocrit percentage (HCT%), mean corpuscular hematocrit (MCH) and serum transferrin saturation percentage (TSAT%) were also observed (Supplemental Fig. 1b). Spleen tissue sections stained with Perl's Prussian blue revealed profound intracellular iron sequestration, indicating severe RES blockade in both *FGFR4*$^{+/+}$ and *FGFR4*$^{-/-}$ mice on adenine (Fig. 1g). Taken together, our data demonstrates that FGF23-FGFR4 signaling does not affect inflammation, the acute phase response or functional iron deficiency and anemia in adenine-induced CKD.

FGF23-FGFR4 signaling does not contribute to hypoferremia following dietary Pi overload

Excess Pi is a hallmark of CKD, but direct pathologic effects of Pi on tissues other than the vasculature are poorly understood (Komaba and Fukagawa, 2016; Scialla and Wolf, 2014). To examine if liver Pi deposition is increased in CKD, we analyzed liver Pi levels in adenine-induced mouse CKD model by colorimetric quantification. Hepatic Pi levels were elevated in

both *FGFR4*$^{-/-}$ and *FGFR4*$^{+/+}$ mice following adenine (Fig. 1h) but less so in *FGFR4*$^{-/-}$ mice when compared to *FGFR4*$^{+/+}$ mice.

To establish whether excess Pi and/or FGF23 contributes to hypoferremia in the absence of CKD, we exposed *FGFR4*$^{+/+}$ and *FGFR4*$^{-/-}$ mice to a graded dietary Pi load for 12 weeks. Serum FGF23 levels increased in both genotypes on 2% Pi and 3% Pi diet, in comparison to mice on 0.7% Pi diet (Fig. 2a). Despite 2% Pi increasing serum FGF23, serum Pi levels significantly increased only on 3% Pi, in comparison to mice fed 0.7% Pi (Fig. 2a). Notably, these serum Pi levels are comparable to the elevated serum Pi levels observed in adenine-induced CKD (Fig. 1b). No significant differences in serum calcium levels were observed between genotypes (Supplemental Fig. 2a), despite elevated Pi levels (Fig. 2a). No pathologic changes were detected in kidneys regardless of genotype as BUN, serum creatinine and kidney tissue sections stained with hematoxylin and eosin (H&E) appeared similar to those of mice on 0.7% Pi (Supplemental Fig. 2b-d). Interstitial fibrosis was not detected in kidneys as shown by Masson's trichrome staining (Supplemental Fig. 2e). These data indicate elevations in serum levels of FGF23 and Pi in mice on 2% Pi or 3% Pi diet are consequences of an increasing dietary Pi load and not renal dysfunction.

As a high Pi diet has been reported to exacerbate inflammation and serum FGF23 levels (Sugihara et al., 2017; Takashi et al., 2019; Yamada et al., 2014), we evaluated gene expression of inflammatory cytokines and acute phase proteins. Compared to 0.7% Pi, liver *Il1b*, *Il6* and *Saa1* transcript levels significantly increased in both *FGFR4*$^{+/+}$ and *FGFR4*$^{-/-}$ mice on 3% Pi, although not on 2% Pi diets (Fig. 2b, c). Liver injury was not detected, as no significant elevations in hepatic alanine aminotransferase (*Alt1*) or aspartate aminotransferase (*Ast1*) mRNA

levels were found on 3% Pi (Supplemental Fig. 3a, b). These data support the notion that dietary Pi overload induces inflammation, but not via FGF23-FGFR4 signaling.

To explain these effects of 3% Pi diet and determine if increased tissue Pi deposition is associated with adverse outcomes, we analyzed the relationship between liver and serum Pi levels in both *FGFR4*$^{+/+}$ and *FGFR4*$^{-/-}$ mice following a graded dietary Pi load. A positive correlation was detected between hepatic and serum Pi levels in both genotypes, beginning with 2% Pi (Fig. 2d). These results show liver Pi deposits increase following elevations in dietary Pi content.

Next, we tested if increased liver Pi accumulation affects correlations between liver Pi and liver *Hamp* mRNA levels, as a high Pi diet induces *Hamp* expression (Nakao et al., 2015). A positive correlation between liver Pi and liver *Hamp* mRNA levels were detected in both *FGFR4*$^{+/+}$ and *FGFR4*$^{-/-}$ mice, again only with diets containing 2% or 3% Pi (Fig. 2e). As liver injury was not detected (Supplemental Fig. 3a, b), these data indicate that elevations in liver *Hamp* mRNA are independent of liver injury and may result from Pi-driven inflammation.

We next explored if increased dietary Pi loading led to changes in hematological responses. Marked reductions in RBC, MCV, hemoglobin and serum iron levels were detected on 3% Pi and were similar in both *FGFR4*$^{+/+}$ and *FGFR4*$^{-/-}$ mice (Fig. 2f). HCT% and MCH were also significantly decreased (Supplemental Fig. 3c). Supporting these findings, spleen tissue sections revealed both *FGFR4*$^{+/+}$ and *FGFR4*$^{-/-}$ mice show increased intracellular iron deposits on 3% Pi (Fig. 2g). Thus, dietary Pi loading causes iron restriction and anemia even in the absence of CKD.

Mouse models of hyperphosphatemia exhibit signs of skeletal muscle wasting which are independent of FGF23-FGFR4 signaling.

As inflammation is a known contributor of muscle wasting (Raj et al., 2008; Schaap et al., 2006; Verzola et al., 2016), and since hyperphosphatemia and excess FGF23 are associated with inflammation, we explored whether hyperphosphatemia contributes to skeletal muscle wasting, and if pathologic FGF23-FGFR4 signaling is involved in these effects. We analyzed skeletal muscle from *FGFR4*$^{+/+}$ and *FGFR4*$^{-/-}$ mice exposed to adenine-induced CKD (Fig. 1) or a graded dietary Pi load (Fig. 2). Examination of skeletal muscle strength indicates that mice on adenine or 3% Pi diet exhibit reduced grip strength in both *FGFR4*$^{+/+}$ and *FGFR4*$^{-/-}$ mice, in comparison to respective control mice (Fig. 3a). A reduction in gastrocnemius mass was also observed (Fig. 3b). Notably, gastrocnemius metallothionein-1 (*Mt1*) transcript levels were significantly elevated in both genotypes following adenine and 3% Pi diets (Supplemental Fig. 4a, b), indicating that either condition fosters skeletal muscle abnormalities.

We next investigated if these muscle deficits resulted from inflammation inducing myostatin and downstream atrophy-related gene programs, as both experimental models display elevated levels of liver *Il1b* and *Il6* (Fig. 1c, Fig. 2b). Compared to respective control mice, gastrocnemius myostatin (*Mstn*) transcript levels were significantly elevated in both *FGFR4*$^{+/+}$ and *FGFR4*$^{-/-}$ mice following adenine or 3% Pi diet (Fig. 3c). Additionally, both genotypes on 2% Pi showed an increased trend in *Mstn* mRNA levels (Fig. 3c). As these findings suggest increased myofibrillar protein degradation, we further analyzed the expression of two specific ubiquitin ligases of muscle-protein breakdown, muscle RING-finger protein 1 (Murf1) and Atrogin-1. Compared with their respective control mice, gastrocnemius *Murf1* and *Atrogin1*

transcript levels were significantly elevated in both *FGFR4*$^{+/+}$ and *FGFR4*$^{-/-}$ mice following adenine and 3% Pi diets (Fig. 3d).

As elevated myostatin and increased myofibrillar protein degradation are features of skeletal muscle wasting, we assessed if these results prompt a shift towards smaller myofibers. Indeed, gastrocnemius tissue sections stained with H&E from *FGFR4*$^{+/+}$ and *FGFR4*$^{-/-}$ mice, on either adenine or 3% Pi diet, showed smaller muscle fiber size compared with controls (Fig. 3e). Taken together, these data suggest skeletal muscle wasting in adenine-induced CKD and hyperphosphatemia does not require FGF23-FGFR4 signaling.

Low Pi feeding limits functional iron deficiency in *COL4A3*$^{-/-}$ (Alport syndrome) mice

Alport (*COL4A3*$^{-/-}$) mice are an established model of progressive CKD which develop hyperphosphatemia with severe inflammation, hypoferremia and anemia (Francis et al., 2019). To test if hyperphosphatemia aggravates these pathologic complications, we exposed *COL4A3*$^{-/-}$ mice to a low Pi diet treatment (0.2% Pi) for 6 weeks. In comparison to wild-type (*COL4A3*$^{+/+}$) mice on normal diet (0.6% Pi), *COL4A3*$^{-/-}$ mice showed renal dysfunction by increased BUN and serum creatinine levels (Fig. 4a). *COL4A3*$^{-/-}$ mice on low Pi diet displayed a reduction in both parameters (Fig. 4a), along with reduced pathologic alterations in kidney morphology (Supplemental Fig. 5a). As compared to wild-type mice, serum levels of FGF23 and Pi significantly increased in *COL4A3*$^{-/-}$ mice on normal diet (Fig. 4b), but less so in *COL4A3*$^{-/-}$ mice on low Pi diet (Fig. 4b).

To identify if a low Pi diet affects inflammation or the acute phase response in Alport mice, we assessed gene expression of inflammatory cytokines and acute phase proteins. Compared to wild-type mice on normal diet, liver *Il1b*, *Il6* and *Saa1* transcript levels were significantly elevated in *COL4A3*$^{-/-}$ mice but much less elevated on 0.2% Pi (Fig. 4c, d). These data support the notion that excess Pi in Alport mice aggravates inflammation.

As our results show that a low Pi diet decreases inflammation, we next explored its impact on functional iron deficiency. Compared to wild-type mice on normal diet, liver *Hamp* transcript levels were significantly elevated in *COL4A3*$^{-/-}$ mice with complete reversal by low Pi diet (Fig. 4e). Assessing hematological responses, *COL4A3*$^{-/-}$ mice on normal diet were anemic, with significant reductions in RBC count, MCV, hemoglobin and serum iron levels (Fig. 4f), as well as in HCT%, MCH and TSAT% (Supplemental Fig. 5b). *COL4A3*$^{-/-}$ mice on normal diet displayed profound intracellular iron sequestration in spleen (Fig. 4g), along with excessive spleen and liver non-heme iron levels (Supplemental Fig. 5c, d). These effects were substantially ameliorated by low Pi diet in *COL4A3*$^{-/-}$ mice, with improved hematologic parameters and reduced iron deposits in spleen (Fig. 4f, g). Non-heme iron levels in spleen and liver were reduced in *COL4A3*$^{-/-}$ mice by treatment, indicating increased iron mobilization and decreased iron restriction (Supplemental Fig. 5c, d). These data indicate that dietary Pi restriction improves hematological responses and alleviates hypoferremia.

As liver Pi accumulation is increased in adenine-induced CKD (Fig. 1h), we next explored if low Pi diet treatment reduces pathologic liver Pi deposits in progressive CKD. Compared to wild-type mice on normal diet, liver Pi levels were increased in *COL4A3*$^{-/-}$ mice and were reduced on low Pi diet (Fig. 4h). Taken together, our data demonstrate that Pi restriction as a dietary intervention, in a genetic model of progressive CKD, reduces pathologic

Pi accumulation in the liver and alleviates the severity of renal injury and functional iron deficiency.

Low Pi feeding counteracts signs of skeletal muscle wasting in *COL4A3*$^{-/-}$ (Alport syndrome) mice

To determine if reducing hyperphosphatemia limits skeletal muscle wasting, an important complication of CKD (Verzola et al., 2018), we analyzed skeletal muscle from wild-type (*COL4A3*$^{+/+}$) and Alport (*COL4A3*$^{-/-}$) mice subjected to either a normal diet (0.6% Pi) or a low Pi diet treatment (0.2% Pi) (Fig. 3). Compared to wild-type mice on normal diet, *COL4A3*$^{-/-}$ mice showed significant reduction in grip strength which was improved by low Pi diet (Fig. 5a). Gastrocnemius mass was also reduced in *COL4A3*$^{-/-}$ mice, and treatment tended to improve muscle weight (Fig. 5b). In particular, gastrocnemius *Mt1* transcript levels were significantly elevated in *COL4A3*$^{-/-}$ mice compared to wild-type mice on normal diet and were reduced by low Pi diet (Supplemental Fig. 4c). These results suggest that Pi restriction as a dietary intervention may improve skeletal muscle abnormalities in CKD. Furthermore, compared to wild-type mice on normal chow, *COL4A3*$^{-/-}$ mice displayed significant elevations in gastrocnemius *Mstn* transcript levels which was reduced by treatment (Fig. 5c). Additionally, *COL4A3*$^{-/-}$ mice on normal diet showed increased gastrocnemius *Murf1* and *Atrogin1* transcript levels, which were also reduced by low Pi diet (Fig. 5d). These data support the notion that dietary Pi restriction, as a treatment in *COL4A3*$^{-/-}$ mice, reduces myostatin synthesis and subsequent atrophy-related gene programs.

As with adenine-induced CKD mice, or mice fed high phosphate diet, gastrocnemius tissue sections from *COL4A3*$^{-/-}$ mice showed smaller muscle fiber size compared to wild-type controls (Fig. 5e). However, *COL4A3*$^{-/-}$ mice fed low Pi diet showed improved muscle fiber size (Fig. 5e). Taken together, these data suggest that hyperphosphatemia affects skeletal muscle wasting in Alport mice, possibly by exacerbating systemic inflammatory cytokine concentrations and their catabolic effects on muscle.

Pi targets hepatocytes and increases expression of inflammatory cytokines and hepcidin

Having shown that inflammation, hypoferremia, and muscle wasting induced by high Pi are independent of FGF23-FGFR4 signaling, we tested if Pi directly affects inflammatory cytokine and hepcidin expression in mouse primary hepatocytes.

We first analyzed the expression profile of the three families of Na/Pi cotransporters (type I - III). Quantitative polymerase chain reaction (qPCR) analysis detected high levels of *Pit1* and *Pit2*, but not *Npt1* and *4*, or *NaPi2a*, *2b* and *2c* (Supplemental Fig. 6a). This analysis indicates that type III Na/Pi cotransporters are the predominant Na/Pi family in primary hepatocyte cultures.

Based on studies demonstrating that high extracellular Pi activates signaling pathways such as MAPK and NFκB (Chavkin et al., 2015; Zhao et al., 2011), we assessed if MAPK, STAT3 and NFκB signaling are activated in cultured hepatocytes in response to treatments with FGF23 or graded concentrations of Pi. Treatment with TNFα or IL6 was used as a positive control for activation of these established networks regulating inflammatory gene expression.

Immunoblot analysis of ERK1/2, STAT3 and NFκB showed that Pi treatments increased phosphorylated NFκB levels without changing total NFκB expression (Fig. 6a). Increased concentrations of Na_2SO_4, a salt generating another anionic species, had no effect on phospho-NFκB levels, indicating this response was specific to elevated Pi and not an unspecific response to increased anions. Pi treatment did not affect pERK1/2 or pSTAT3, and FGF23 had no effect on any of the pathways examined.

We next analyzed gene expression by qPCR of inflammatory cytokines and acute phase proteins in isolated hepatocytes treated with increasing concentrations of Pi or Na_2SO_4 with LPS and IL6 treatments used as positive control. Elevations in *Il1b*, *Il6* and *Saa1* transcript levels were noted not only following LPS and IL6 but also Pi treatments (Fig. 6b, c). Treatments with Na_2SO_4 had no effect on gene expression. As inflammation is a known mediator of hepcidin synthesis, we analyzed *Hamp* mRNA levels. LPS, IL6 and Pi treatments all elevated *Hamp* transcript levels when compared to control (Fig. 6d). These data indicate high extracellular Pi can act on hepatocytes to increase the synthesis of inflammatory cytokines and hepcidin.

Given that inflammation and NFκB signaling regulate PiT1 expression (Koumakis et al., 2019) and primary hepatocytes express *Pit1* and *Pit2* (Supplemental Fig. 6a), we examined if *Pit1* and/or *Pit2* mRNA levels were altered following LPS, IL6 or Pi treatment. Expression analysis showed that Pi significantly increased *Pit1* transcript levels in a dose-dependent manner but had no effect on *Pit2* expression (Fig. 6e, Supplemental Fig. 6b). To determine if this result is an action of hepatocytes sensing high extracellular Pi, we cotreated hepatocytes with phosphonoformic acid (PFA), a compound which is reported to inhibit chemisorption of calcium-Pi clusters, as aggregate formation is a byproduct of increased extracellular Pi (Villa-

Bellosta et al., 2007; Villa-Bellosta and Sorribas, 2009). In the presence of PFA, Pi-induced *Pit1* expression was reduced compared to vehicle-treated control cells (Fig. 6f). Interestingly, PFA also altered the effects of LPS and IL6 on *Pit1* expression. To confirm whether inhibiting high extracellular Pi and/or aggregate byproducts disrupts downstream actions of increased extracellular Pi, we co-treated hepatocytes with Pi and PFA, and observed that PFA interfered with Pi-induced effects on phospho-NFκB levels without changing total NFκB expression (Fig. 6g).

Furthermore, when isolated hepatocytes were treated with either LPS, IL6 or Pi in the presence or absence of PFA, the significant elevations in *Il1b*, *Il6*, *Saa1* and *Hamp* transcript levels following Pi treatments were reversed in the presence of PFA (Fig. 6h-j). Interestingly, PFA slightly altered the effects of LPS on *Il6* expression and IL6 on *Hamp* expression (Fig. 6h-j). Taken together, our results indicate that in primary hepatocyte cultures type III Na/Pi cotransporters are predominant, and that increased extracellular Pi activates NFκB signaling, increases PiT1 expression and induces inflammatory cytokine and hepcidin production.

Pi induces hepcidin expression via paracrine IL1β and IL6 signaling

Next, we explored if NFκB is a necessary mediator for inflammatory cytokine and hepcidin regulation by high extracellular Pi *in vitro*. We treated mouse primary hepatocytes with either LPS or graded Pi concentrations in the presence or absence of a selective NFκB pharmacologic inhibitor, BAY 11-7082 (Koumakis et al., 2019; Pierce et al., 1997). Significant elevations in *Il1b*, *Il6* and *Hamp* mRNA levels were detected following LPS or Pi treatments, and these were

362 attenuated by BAY 11-7082 (Fig. 7a-b). Similar effects of BAY 11-7082 on *Saa1*, *Haptoglobin*
363 and *Pit1* mRNA expression were also observed, corroborating reports that NFκB directly
364 regulates PiT1 abundance (Supplemental Fig. 7a-c).

365 As inflammation directly regulates hepcidin, we explored if Pi-induced hepcidin
366 expression is a response resulting from direct or indirect actions of NFκB. Testing indirect
367 effects, we cotreated primary hepatocytes with either LPS or graded Pi concentrations in the
368 presence or absence of anti-IL1β antibody, anti-IL6 antibody or both neutralizing antibodies in
369 combination. Expression analysis detected significant elevations in *Hamp* mRNA levels
370 following LPS or Pi treatments and was blunted by addition of either antibody alone or in
371 combination (Fig. 7c). To ensure treatments generated endogenous IL1β and IL6 protein, we
372 analyzed *Saa1* and *Haptoglobin* mRNA expression, as both genes are regulated by IL1β and IL6
373 (Zhou et al., 2016). Compared to vehicle-treated control cells, *Saa1* and *Haptoglobin* transcript
374 levels were reduced in the presence of either antibody alone or in combination, following LPS or
375 Pi treatment (Supplemental Fig. 7d, e). Collectively, these results show Pi-mediated hepcidin
376 production in cultured hepatocytes is a result of NFκB amplifying PiT1 expression, which in
377 turn, might intensify high extracellular Pi to augment NFκB regulated inflammatory gene
378 programs, prompting the induction of required cytokines IL1β and IL6 to mediate hepcidin
379 production.

380

381 **Discussion**

We report that hyperphosphatemia, either as a result of adenine-induced CKD or dietary Pi excess, increases inflammation to exacerbate anemia and skeletal muscle wasting. These complications are associated with increased liver Pi levels, which correlated with serum Pi concentrations. Supplying a low Pi diet treatment to Alport mice, a genetic model of CKD, results in beneficial outcomes that reduce functional iron deficiency and skeletal muscle wasting. Furthermore, our mechanistic *in vitro* studies indicate that Pi elevations induce hepatic production of IL6 and IL1β to increase hepcidin expression in hepatocytes, a potential causative link between hyperphosphatemia, anemia, and skeletal muscle dysfunction.

Previously, we reported pathologic FGF23-FGFR4 signaling might contribute to excess inflammatory mediators (Singh et al., 2016), and we now followed up on the FGF23 inflammatory role in clinically-relevant CKD models in vivo. Here, we examined wild-type ($FGFR4^{+/+}$) and constitutive FGFR4 knockout ($FGFR4^{-/-}$) mice subjected to adenine diet or a graded dietary Pi load. We found that on adenine, both $FGFR4^{+/+}$ and $FGFR4^{-/-}$ mice show comparable macroscopic parameters (Table 1) and degrees of functional iron deficiency (Fig. 1). These findings coincide with greater levels of liver Pi, which raises the possibility that pathologic Pi deposits, in tissues apart from the vasculature, may contribute to additional complications in CKD (Komaba and Fukagawa, 2016).

Clinical reports indicate CKD patients have dysregulated Pi handling (Chang et al., 2014; Isakova et al., 2009) and together with the consumption of foods and drinks rich in Pi-based additives, such as in a Westernized diet, extra-renal Pi accumulation may occur (Isakova et al., 2008). A recent study utilizing animal models supports this postulate, demonstrating that excess Pi leads to depositions into tissues such as the vasculature (Zelt et al., 2019). Moreover, a recent report indicates the major source of body Pi removed during hemodialysis in CKD patients, is

405 from cells releasing intracellular Pi (Chazot et al., 2020). As the serum Pi compartment
406 represents a small fraction of total body Pi, and the uptake of excess Pi by tissues is recognized
407 as a detrimental trigger, it is important to examine the degree of pathologic Pi accumulation in
408 non-vascular tissue and whether it exacerbates complications in CKD, such as anemia and
409 muscle wasting.

410 We employed a graded Pi diet to study the effects of excess Pi on the liver (Fig. 2).
411 Studies show conflicting results towards renal and liver health, following supplementation of a
412 high Pi diet (Baquerizo et al., 2003; Haut et al., 1980; Ugrica et al., 2021). In our study, no
413 significant changes in macroscopic parameters were observed following dietary Pi overload
414 (Table 2). Also, no pathologic changes in kidney (Supplemental Fig. 2) or liver were detected
415 (Supplemental Fig. 3). However, mice on a 3% Pi diet exhibit increased liver inflammation and
416 *Hamp* expression, which corroborates previous observation that high dietary Pi influences
417 hepcidin production (Nakao et al., 2015). These results coincide with positive correlations
418 between liver Pi and liver *Hamp* mRNA expression, with onset of this correlation preceding
419 significant elevations in serum Pi. Despite these data suggesting that liver Pi influences liver
420 hepcidin production, our finding might indicate that increased extra-renal Pi accumulation
421 provides a reservoir for storing excess Pi until tissue accumulation achieves saturation, in which
422 case the serum Pi compartment then gradually rises, resulting in hyperphosphatemia.
423 Furthermore, our data suggest that prolonged exposure to Pi, if not maintained in adequate
424 quantities, might trigger pathologic outcomes, as mice on 3% Pi show a noticeable degree of
425 hypoferremia. None of the observed effects of the high Pi diet were mediated by FGFR4, as
426 *FGFR4*$^{-/-}$ mice were comparable to wild-type mice in all the parameters measured. However, this
427 work cannot exclude the potential of alternative FGFRs which might mediate the effects of

428 excess FGF23 towards functional iron deficiency following either adenine or 3% Pi diet, as a
429 recent report exhibits the utilization of a single intraperitoneal injection of FGF23 blocking
430 peptide was sufficient to rescue anemia (Agoro et al., 2018).

431 Excess dietary Pi was shown to directly exacerbate intestinal inflammation in a model of
432 experimental colitis (Sugihara et al., 2017) and that reducing dietary Pi provides beneficial
433 outcomes towards systemic inflammation, accelerated aging, and survival, as demonstrated in a
434 model of senescence (Morishita et al., 2001). We likewise observed increased inflammation in
435 our hyperphosphatemic mouse models. Inflammatory cytokines can directly target skeletal
436 muscle cells to induce muscle wasting by increasing myostatin production (Zhang et al., 2013),
437 which both together, enhances protein degradation and reduces protein synthesis, as CKD
438 illustrates catabolic conditions which are attributable to the vicious cycle generated between
439 mineral dyshomeostasis and inflammation (Czaya and Faul, 2019b). We indeed observed
440 skeletal muscle wasting in adenine-induced CKD, high phosphate diet, and genetic model of
441 CKD. Ablation of FGFR4 in mice did not improve skeletal muscle function following adenine or
442 3% Pi diets, suggesting hyperphosphatemia rather than pathologic FGF23-FGFR4 signaling
443 might be the cause of skeletal muscle abnormalities (Fig. 3). This hypothesis is supported by
444 reports demonstrating excess Pi influences skeletal muscle dysfunction (Acevedo et al., 2016;
445 Chen et al., 2018; Chung et al., 2020), although it is possible additional FGFR isoforms directly
446 promote skeletal muscle wasting due to excess FGF23 following adenine or high Pi diet.
447 However, a recent report suggests that FGF23 does not directly affect skeletal muscle
448 dysfunction (Avin et al., 2018).

449 To assess whether reducing hyperphosphatemia can improve inflammation, anemia, and
450 skeletal muscle wasting, we exposed Alport mice, a genetic model of progressive CKD, to a low

Pi diet treatment. Indeed, despite severe elevations in serum FGF23, dietary Pi restriction limited functional iron deficiency (Fig. 4). Our data also shows liver Pi levels were reduced in Alport mice following low Pi diet treatment, in comparison to Alport mice on normal diet. These findings provide strong evidence that hyperphosphatemia, specifically pathologic liver Pi accumulation, rather than pathologic FGF23-FGFR4 signaling, might exacerbate inflammation and hypoferremia. Skeletal muscle function and mass were also improved by a low Pi diet in Alport mice, along with decreased expression of muscle myostatin and atrophy-related gene programs, culminating in larger myofiber size. These findings suggest the contribution of hyperphosphatemia to skeletal muscle wasting may result from an indirect mechanism that regulates inflammatory cytokines and their pleotropic activities, such as increased liver-derived IL1β and IL6, which might increase overall systemic levels that effectively target skeletal muscle. Despite this postulate, further work will be needed to determine if high extracellular Pi directly targets skeletal muscle cells to affect muscle function. Nonetheless, these data add to the growing list of adverse outcomes of Pi toxicity such as gingivitis, accelerated aging, vascular calcification and tumorigenesis (Erem and Razzaque, 2018). Furthermore, Alport mice on low Pi diet treatment displayed a reduced degree of pathologic kidney function, alterations in kidney morphology, and macroscopic parameters (Fig. 4, Supplemental Fig. 5, Table 3). Thus, we cannot exclude that these beneficial outcomes in Alport mice observed on treatment may be a repercussion of slightly improved kidney function, as a recent report demonstrates elevated Pi concentrations directly affect proximal tubular function (Shiizaki et al., 2021).

Importantly, we identify a molecular mechanism that potentially links hyperphosphatemia to anemia and skeletal muscle dysfunction. Utilizing mouse primary hepatocytes, we demonstrate high extracellular Pi activates NFκB signaling and leads to

subsequent inflammatory cytokine and hepcidin production (Fig. 6). Employing PFA, a compound reported to reduce calcium-Pi deposition and cluster formation, as aggregates are a byproduct of increased extracellular Pi (Villa-Bellosta et al., 2007; Villa-Bellosta and Sorribas, 2009), we confirm NFκB activation is a direct action of Pi targeting hepatocytes, which prompts subsequent *Pit1* mRNA expression, as observed from our BAY 11-7082 findings. This high extracellular Pi-NFκB signaling axis is observed in other reservoirs such as vascular smooth muscle cells and ex vivo kidney slices (Rodríguez-Ortiz et al., 2020; Voelkl et al., 2018; Zhao et al., 2011). Although this reaffirms NFκB directly influences PiT1 levels (Koumakis et al., 2019), it does not identify if our observations are dependent or independent of Pi translocation, as extracellular Pi might associate with various PiT1 extracellular regions to influence PiT1-PiT1 homodimerization, PiT1-PiT2 heterodimerization or a conformational change in PiT1 to initiate the activation of selected binding partners which mediate downstream signaling events (Bon et al., 2018; Forand et al., 2016). In addition to this amplified hepatic PiT1 abundance and recognition of NFκB as a necessary mediator of high extracellular Pi in hepatocytes, we show that the effect of Pi on hepcidin requires the indirect actions of NFκB and biological activities of endogenous IL1β and IL6 proteins secreted by hepatocytes, as elucidated by our cell-based neutralization assay of these targeted cytokines (Fig. 7). Based on these findings, we speculate increased liver Pi deposits might underlie a clinical association between elevated body Pi and inflammation, where the prolonged duration of tissue accumulation permits Pi in the liver to directly target hepatocytes to induce inflammatory gene programs and hepcidin expression, contributing to hypoferremia. This could explain associations of inflammation and anemia in FTC patients, in addition to patients with and without CKD, before they exhibit hyperphosphatemia (Ramnitz et al., 2016; Tran et al., 2016; Wojcicki, 2013).

Our study has some limitations. Although we confirm hyperphosphatemia affects specific complications, our study does not specifically address the actions of certain aggregate byproducts formed by increased extracellular Pi. Nonetheless, this principal emphasis on elevations in plasma Pi concentrations will ultimately impact the formation of byproducts. Notably, the identification of the specific Pi sensor which mediates our observed hepatic Pi actions are not definite and remains to be defined with our ongoing studies. Moreover, our study does not address the specific actions of hyperphosphatemia on bone metabolism. As bone is a reservoir of extracellular Pi, potential alterations in bone health could relay a crosstalk between bone, liver and/or skeletal muscle, which might contribute to our reported observations.

In summary, we investigated whether hyperphosphatemia and/or pathologic FGF23-FGFR4 signaling aggravates inflammation, anemia, and skeletal muscle wasting. We establish hyperphosphatemia, as found in dietary Pi overload or in CKD, is a detrimental trigger which activates hepatic NFκB signaling to stimulate an inflammatory response, which in turn, exacerbates hypoferremia and widespread complications such as skeletal muscle wasting. Notably, these findings are independent of pathologic FGF23-FGFR4 signaling. Clinical studies have demonstrated conflicting outcomes with traditional Pi binders in individuals with non-dialysis-dependent CKD, but modern Pi binders, such as ferric citrate, demonstrate greater efficacy (Francis et al., 2019; Toussaint et al., 2020), and are being evaluated for their effect on CKD comorbidities. Furthermore, reports assessing dietary Pi restriction in animal models are scarce. Our current experimental data suggests hyperphosphatemia, in itself, is pathologic and demands further attention for alternative strategies to resolve current ineffective approaches. Treatments, such as pharmacologic inhibition of type II Na/Pi cotransporters, hold potential for therapeutic actions (Clerin et al., 2020; Thomas et al., 2019) but do not aim at altered mineral

metabolism. Using *in vitro* studies and complementary animal models, we provide insights regarding the interconnection between altered mineral metabolism and common complications. Dietary Pi restriction might alleviate these sequelae, if sustained effectively as a clinical treatment. By elucidating direct inflammatory actions of high extracellular Pi on hepatocytes, we expose additional adverse outcomes of hyperphosphatemia, besides vascular calcification. These findings may yield new targets for therapeutic development, with emphasis on hepatic Pi actions. Moreover, as studies indicate anti-FGFR4 therapy may be beneficial towards cardiomyopathy (Grabner et al., 2015), our data suggests these same beneficial outcomes for inflammation, anemia, and skeletal muscle wasting would not apply. Altogether, our study features a possibility to improve CKD patient survival and specific rare genetic disorders, such as FTC, by limiting excess body Pi.

Materials and Methods

Materials. Recombinant proteins used are mouse FGF23 (2629-FG, R&D Systems), mouse TNFα (410-MT, R&D Systems) and mouse IL6 (406-ML, R&D Systems). This FGF23 peptide contains an arginine to glutamine amino acid substitution at position 179 which yields it resistant to furin protease-mediated degradation, thus prolonging its half-life. Lipopolysaccharide (LPS) (tlrl-3pelps, Invivogen) was used as endotoxin. Sodium phosphate dibasic anhydrous (Na_2HPO_4) (BP332-500, Fisher Scientific) and sodium phosphate monobasic anhydrous (NaH_2PO_4) (BP329-1, Fisher Scientific) were used to prepare a 1 M stock sodium phosphate buffer solution containing 500 mM Na_2HPO_4 and 500 mM NaH_2PO_4 at an adjusted pH of 7.4. Sodium sulfate

542 (Na_2SO_4) (239313, Sigma-Aldrich) was used to prepare a 1 M stock sodium sulfate buffer
543 solution at an adjusted pH of 7.4. Phosphonoformic acid (PFA) (P6801, Sigma-Aldrich) and
544 BAY 11-7082 (S2913, Selleckchem) were used as agents to elucidate underlying signal
545 transduction mechanisms. Anti-IL6 (MP5-20F3, R&D Systems) and anti-IL1β (AF-401-NA,
546 R&D Systems) were used as antibodies in a cell-based assay to neutralize the biological activity
547 of targeted cytokines.

548 **Mice.** Animal studies were performed in the conformity with applicable laws and guidelines and
549 were approved by the Animal Research Committee at the University of Alabama Birmingham
550 School of Medicine (UAB). Studies were performed using male mice and were maintained on a
551 NIH 31 rodent diet (Harlan Teklad) and fed *ad libitum*, unless otherwise indicated. Constitutive
552 FGF Receptor 4 null (*FGFR4*$^{-/-}$) mice (Weinstein et al., 1998) were maintained on a C57BL/6
553 background. Constitutive *COL4A3*$^{-/-}$ null (Alport) mice (Cosgrove et al., 1996) were maintained
554 on a mixed Sv129/C57BL/6 background. Both mouse models were housed in our UAB rodent
555 facility, in a heterozygous breeding state.

556 For experiments exploring the contribution of pathologic FGF23-FGFR4 signaling to
557 CKD-associated pathologies, 10- to 14-week-old *FGFR4*$^{-/-}$ mice and corresponding wild-type
558 littermates were placed on a customized diet containing 0.2% adenine (TD.140290, Envigo) for 6
559 weeks, switched to a customized diet containing 0.15% adenine (TD.170304, Envigo) for 2
560 weeks and transitioned back to the customized 0.2% adenine diet for an additional 6 weeks.
561 Wild-type littermates placed on a customized control diet (TD.170303, Envigo) served as
562 controls. All experimental groups were permitted a one-week dietary acclimation period, using
563 the customized control diet. After dietary acclimation, mice were unbiasedly assigned to either
564 the customized control diet or customized adenine diet. After the 14-week duration, mice were

565 euthanized under 2.5% isoflurane anesthesia and samples were prepared as described in
566 supplemental materials and methods. This experimental timeline is in accordance with previous
567 studies (Noonan et al., 2020; Taylor et al., 2019). Adenine is known to induce kidney tubule-
568 interstitial damage and is considered a dietary model of CKD.

569 For experiments testing the contribution of pathologic FGF23-FGFR4 signaling to
570 systemic effects of a graded dietary phosphate load, 10- to 14-week-old *FGFR4*$^{-/-}$ mice and
571 corresponding wild-type littermates were unbiasedly assigned and fed a customized 0.7%
572 phosphate diet (TD.180287, Envigo), a customized 2.0% phosphate diet (TD.08020, Envigo) or a
573 customized 3.0% phosphate diet (TD.180286, Envigo) for 12 weeks. Wild-type littermates
574 placed on the customized 0.7% phosphate diet served as controls. At end of the experimental
575 period, mice were euthanized under 2.5% isoflurane anesthesia and samples were prepared as
576 described in supplemental materials and methods.

577 For experiments investigating the contribution of hyperphosphatemia to CKD-associated
578 pathologies, 4-week-old Alport mice and corresponding wild-type littermates were unbiasedly
579 assigned and fed a customized 0.6% phosphate diet (TD.200407, Envigo) or a customized 0.2%
580 phosphate diet (TD.200406, Envigo) as treatment for 6 weeks. Constitutive *COL4A3*$^{-/-}$ null mice
581 are considered a genetic model of Alport syndrome and progressive CKD. When maintained on a
582 mixed Sv129/C57BL/6 background, Alport mice die at 10 weeks of age due to rapid renal injury.
583 Wild-type littermates placed on the customized 0.6% phosphate diet served as controls. At 10
584 weeks of age, mice were euthanized under 2.5% isoflurane anesthesia and samples were
585 prepared as described in supplemental materials and methods. A detailed description of diet
586 compositions is indicated in Tables 4, 5 and 6. All experimental group numbers were pre-

587 determined on the basis of experience from previous publications. Investigators were not blinded
588 to mouse genotypes.

589 **Serum Chemistry.** Mouse blood was collected by cardiac puncture and transferred into
590 microvette serum gel tubes (20.1344, Sarstedt). Samples were then centrifuged at 10,000 g for 5
591 minutes at room temperature. Serum supernatants were harvested and stored at -80°C. Clinical
592 chemistry analyses were performed by the Animal Histopathology & Laboratory Medicine Core
593 at the University of North Carolina, which is supported in part by an NCI Center Core Support
594 Grant (5P30CA016086-41) to the UNC Lineberger Comprehensive Cancer Center. Serum intact
595 FGF23 was assessed using ELISA (60-6800, Quidel).

596 **Grip-strength test.** Muscle strength was assessed using a Chatillon DFE series digital force
597 gauge (E-DFE-200, Chatillon) with a metal grid adaptor, provided by the Behavioral Assessment
598 Core at UAB. Mice were allowed to grip the metal grid with fore- and hindlimbs and then gently
599 pulled backwards by their tail, until mice could not grip the metal grid. Each mouse was given 10
600 trials, excluding the highest and lowest values. These 8 trials were then averaged. These
601 averaged values are used to represent the muscle grip-strength of each individual mouse.
602 Investigators were blinded to each experimental group.

603 **Mouse tissue collection.** Unless otherwise indicated, tissues were excised, weighed and either
604 immediately flash frozen in liquid nitrogen or fixed for histologic examination. Organ and
605 gastrocnemius weights were measured with an OHAUS scout portable balance (SJX323N/E).

606 **Histology.** Spleen, kidney and gastrocnemius tissues were fixed in 10% formalin solution for 24
607 hours, transferred into 70% ethanol and subjected to paraffin embedding (IDEXX). Spleen,
608 kidney and gastrocnemius sections were cut and either stained with Perl's Prussian blue, H&E or

609 Masson's trichrome (IDEXX) and used for representative images. Images were captured on a
610 Keyence BZ-X800 fluorescent microscope with a 20x objective lens.

611 **Tissue phosphate quantifications.** To quantify liver phosphate concentrations in mouse tissue,
612 liver samples were weighed, homogenized in protein precipitation solution (0.53N HCL, 5.3%
613 trichloroacetic acid (TCA)), boiled for 30 minutes at 95°C and cooled in room temperature water
614 for 2 minutes. Samples were then centrifuged at 13,300 g for 30 minutes at 4°C. Supernatants
615 were collected and subjected to colorimetric phosphate quantifications (ab65622, Abcam)
616 according to the manufactures' instructions.

617 **Tissue iron quantifications.** To quantify non-heme iron concentrations in mouse tissues, spleen
618 and liver samples were weighed, homogenized in protein precipitation solution (0.53N HCL,
619 5.3% trichloroacetic acid (TCA)), boiled for 30 minutes at 95°C and cooled in room temperature
620 water for 2 minutes. Samples were then centrifuged at 13,300 g for 10 minutes at room
621 temperature. Supernatants were harvested and subjected to colorimetric iron quantifications
622 (157-30, Sekisui Diagnostics) according to the manufactures' instructions.

623 **Measurement of hematologic parameters and iron levels.** Mouse blood was collected by
624 cardiac puncture, transferred into microvette EDTA tubes (20.1341, Sarstedt), inverted to
625 prevent clotting and stored at 4°C prior to shipment. Complete blood counts were measured by
626 the Animal Histopathology & Laboratory Medicine Core at the University of North Carolina. In
627 addition, serum supernatants were analyzed for iron and total iron binding capacity (TIBC)
628 concentrations. Transferrin saturation percentage (TSAT%) = (serum iron/TIBC) × 100.

629 **Isolation and cultivation of mouse primary hepatocytes.** Hepatocytes were isolated from 10-
630 to 14-week-old male wild-type C57BL/6J mice, which were anesthetized and placed on a 37°C

heated surface to maintain adequate body temperature. Ventral laparotomy from the pubis to the cranial border of the liver was performed and the abdominal wall was incised to both sides, caudal of the diaphragm, exposing the inferior vena cava (IVC). Following suprahepatic diaphragm incision and surgical silk (5/0) ligation of the thoracic IVC, the infrarenal IVC was cannulated using a 24-gauage shielded catheter (381412, BD) attached to a perfusion line. A peristaltic pump was utilized to perfuse the liver with 30 mL of liver perfusion medium (17701-038, Gibco) followed by 30 mL of liver digest medium (17703-034, Gibco), both pre-warmed in a 37°C water bath. The portal vein was incised to route consecutive retrograde perfusion through the liver at a rate of 3 mL/min until each solution was empty. Next, the digested liver was excised, transferred into a 10-centimeter dish containing hepatocyte wash medium (17704-024, Gibco) and was minced within a cell culture hood. The mixture was then filtered through a 70 μm nylon cell strainer (352350, Falcon) using a 20 mL plastic serological pipette into a 50 mL polypropylene conical tube (352098, Falcon) to remove debris. Cells were washed twice with chilled hepatocyte wash medium with centrifugation at 60 g for 3 minutes at 4°C to allow a soft separation of parenchymal cells from nonparenchymal cells. To enrich the hepatocyte cell population, the cell pellet was resuspended and inverted 4 times in 20 mL of chilled 36% iso-osmotic percoll gradient solution (P1644, Sigma-Aldrich) (percoll gradient solution: William's E medium solution (4 parts: 6 parts)) and centrifuged at 200 g for 7 minutes at 4°C. The enriched hepatocyte population was resuspended in 10 mL of chilled hepatocyte wash medium and subjected to two washes with centrifugation at 60 g for 2 minutes at 4°C. The washed pellet was resuspended in 12 mL of warm William's E medium (12551-032, Gibco) supplemented with primary hepatocyte thawing and plating supplements (CM3000, Gibco), counted in a hemocytometer after staining with trypan blue (25900Cl, Corning), seeded at a density of

$2.5x10^5$ cells/6-well or $1.0x10^5$ cells/12-well on plates coated with 100 μg/mL of collagen type 1 (354236, Corning) and allowed to adhere for 4 hours in a humidified 5% CO_2 incubator at 37°C. After this attachment period, medium was exchanged with fresh warm William's E medium solution supplemented with primary hepatocyte maintenance supplements (CM4000, Gibco) and incubated overnight in a humidified 5% CO_2 incubator at 37°C. Next morning, media was exchanged with fresh warm DMEM (26140079, Gibco) supplemented with 1x Penicillin/Streptomycin (15140122, Gibco) and incubated for 6 hours in a humidified 5% CO_2 incubator at 37°C. This 6-hour serum-starvation period allows cells to synchronize to an identical cell cycle arrest phase, thus eliminating the potential impact between contrasting cell cycles and a cells overall response to exogenous treatment, as serum contains various growth factors and cytokines which promote the activation of signal transduction pathways related to cell proliferation and survival.

Cell culture. Hepatocytes were isolated, cultivated and serum starved as described in supplemental methods. For experiments investigating the activation of signal transduction mediators, cells were seeded on 6-well collagen-coated plates and treated with either TNFα [100 ng/mL], IL6 [50 ng/mL], FGF23 [25 ng/mL] or appropriate amounts of sodium phosphate [1 M; pH 7.4] and sodium sulfate [1 M; pH 7.4] buffers to produce final desired concentrations and incubated for 30 minutes in a humidified 5% CO_2 incubator at 37°C. DMEM supplemented with 1x Penicillin/Streptomycin, which contains ~ 1 mM phosphate, served as a reference control (Ctrl). Sodium sulfate served as a negative control in response to increased anions.

For experiments analyzing expression levels of specific target genes, cells were seeded on 12-well collagen-coated plates and treated with either LPS [100 ng/mL], IL6 [50 ng/mL] or

676 appropriate amounts of sodium phosphate [1 M; pH 7.4] and sodium sulfate [1 M; pH 7.4]
677 buffers to produce final desired concentrations and incubated for 24 hours in a humidified 5%
678 CO_2 incubator at 37°C. As described above, DMEM with 1x Penicillin/Streptomycin served as a
679 reference control (Ctrl) and sodium sulfate served as a negative control.

680 For experiments investigating the role of high extracellular phosphate, cells were seeded
681 on either 6-well or 12-well collagen-coated plates and pre-incubated for 1 hour with or without
682 the addition of PFA [1 mM] in a humidified 5% CO_2 incubator at 37°C. Cells were then either
683 treated for 30 minutes to assess NFκB activation or treated for 24 hours to analyze expression
684 levels of specific target genes, and incubated accordingly in a humidified 5% CO_2 incubator at
685 37°C. Specific treatments were conducted with factors described above. DMEM with 1x
686 Penicillin/Streptomycin served as a reference control (Ctrl).

687 For experiments analyzing the participation of NFκB signaling, cells were seeded on 12-
688 well collagen-coated plates and pre-incubated for 1 hour with or without the addition of BAY
689 11-7082 [20 μM] in a humidified 5% CO_2 incubator at 37°C. Cells were then treated and
690 incubated for 24 hours in a humidified 5% CO_2 incubator at 37°C to analyze expression levels of
691 specific target genes. Specific treatments were conducted with factors described above. DMEM
692 with 1x Penicillin/Streptomycin served as a reference control (Ctrl). Total protein lysates were
693 prepared from 30-minute treatments as described below. Total RNA was prepared from 24-hour
694 treatments as described below. All 24-hour treatments were supplemented with 0.70% FBS
695 (CM3000, Gibco).

696 **Cytokine neutralization.** Hepatocytes were seeded on 12-well collagen-coated plates, cultivated
697 and serum starved as described in supplemental methods. Primary mouse hepatocytes were

treated for 24 hours to analyze expression levels of specific target genes with either LPS [100 ng/mL] or appropriate amounts of sodium phosphate buffer [1 M; pH 7.4] to produce a final desired phosphate concentration and incubated accordingly in a humidified 5% CO_2 incubator at 37°C. Treatments were performed with or without the addition of neutralizing antibodies against IL6 [6 μg/mL] and/or IL1β [6 μg/mL] as indicated. Total RNA was prepared from treatments as described below. All treatments were supplemented with 0.70% FBS (CM3000, Gibco).

RNA isolation and quantification. Total RNA was extracted from liver and cultured hepatocytes using a RNeasy Plus Mini Kit (74136, Qiagen) and from gastrocnemius tissue using a RNeasy Plus Universal Mini Kit (73404, Qiagen) following the manufactures' instructions. Employing a two-step reaction method, 1 μg of total RNA was reverse transcribed into cDNA using iScript Reverse Transcription Supermix (1708840, Bio-Rad). Quantitative PCR was performed with 100 ng of cDNA, SsoAdvanced Universal SYBR Green Supermix (172-5272, Bio-Rad) and sequence specific primers (as indicated in Table 7). Samples were run in duplicate on a CFX96 Touch Real-Time Detection Instrument (1855196, Bio-Rad). Amplification was performed in forty cycles (95°C, 30 seconds; 98°C, 15 seconds; 60°C, 30 seconds; 65°C, 5 seconds). The generated amplicon was systematically double-checked by its melting curve. Relative gene expression was normalized to expression levels of housekeeping genes *18S rRNA* (for *in vitro* studies) or *Gapdh* (for *in vivo* studies). Results were evaluated using the $2^{-\Delta\Delta Ct}$ method and expressed as mean ± SEM.

Protein isolation and Immunoblotting. Total protein was extracted from cells which were placed on ice and scraped from 6-well or 12-well plates, using a 300 μL or 150 μL volume of RIPA lysis buffer (50 mM Tris-HCl pH 7.5, 200 mM NaCl, 1% Triton X-100, 0.25%

720 deoxycholic acid, 1 mM EDTA, 1 mM EGTA) respectively, with addition of protease inhibitor
721 (11836153001, Roche) and phosphatase inhibitors (P5726, P0044, Sigma-Aldrich). Cell lysates
722 were then incubated on ice for 30 minutes and cleared by centrifugation at 13,000 g for 30
723 minutes at 4°C. Supernatants were collected and protein was quantified using a Pierce BCA
724 Protein Assay Kit (23225, Thermo Fisher Scientific).

725 Following protein quantification, supernatants were appropriately aliquoted and
726 suspended in volumes of laemmli sample buffer (1610747, Bio-Rad) with β-mercaptoethanol
727 (1610710, Bio-Rad) as reducing agent, denatured at 100°C for 5 minutes and stored at -80°C.
728 Protein samples [20 μg of cellular protein] were loaded onto 8% or 10% SDS polyacrylamide
729 gels and separated by SDS-PAGE. Polyacrylamide gels were run in 1x Tris/Glycine/SDS buffer
730 (1610732, Bio-Rad) at 20 mA per gel and stopped when sample dyes reached the end of the gels.
731 Proteins were electroblotted onto PVDF membranes (IPVH00010, Merck Millipore) via a semi-
732 dry cassette (1703940, Bio-Rad) in 1x Tris/Glycine Buffer (1610734, Bio-Rad) with 20%
733 methanol at 20 V for 1 hour. Membranes were then blocked in 5% nonfat dry milk with 0.5%
734 Tween 20 diluted in 1x Tris buffered saline (TBS) pH 7.5 for 1 hour and probed with primary
735 antibodies at 1:1,000 against specific antigens overnight at 4°C. ERK1/2 (4695, Cell Signaling),
736 STAT3 (4904, Cell Signaling), NFκB (8242, Cell Signaling) and β-actin (4970, Cell Signaling)
737 primary antibodies were used in 1x TBS with 5% nonfat dry milk and 0.5% Tween 20. Phospho-
738 ERK1/2 (9101, Cell Signaling), phospho-STAT3 (9145, Cell Signaling) and phospho-NFκB
739 (3033, Cell Signaling) primary antibodies were used in 1x TBS with 5% BSA and 0.5% Tween
740 20.

Next day, membranes were subjected to three wash periods for 5 minutes in 1x TBS with 0.5% Tween and then probed with horseradish peroxidase–conjugated goat anti-mouse or goat anti-rabbit secondary antibodies at 1:2,500 (W4021, W4011, Promega) in 1x TBS with 5% nonfat dry milk and 0.5% Tween at room temperature for 1 hour. Membranes were then subjected to three wash periods for 10 minutes in 1x TBS with 0.5% Tween at room temperature. Horseradish peroxidase activity was detected using enhanced chemiluminescence detection solution (RPN2106, GE Healthcare) and imaged on an SRX-101A X-ray film developer. All immunoblots were repeated with a minimum of three independent trials, with comparable results.

Statistics. Data organization, scientific graphing and statistical significance of differences between experimental groups were performed by using GraphPad Prism (version 9.0.0). All results are expressed as mean ± SEM. Depending on number of experimental groups and factors analyzed, we performed a two-way ANOVA followed by a post-hoc Tukey test (for studies affected by 2 factors) or in the form of a one-way ANOVA (for studies measuring variance in 3 groups or more). Correlation and slope analyses were examined by simple linear regression. Statistical significance was set at a P value of less than or equal to 0.05. Sample size was determined on the basis of sample availability, prior experimental studies performed in our laboratory and from prior literature. No formal randomization was used in any experiment. For *in vivo* experiments, animals were unbiasedly assigned into different experimental groups, regardless of genotype. Group allocation was not performed in a blinded manner. Whenever possible, investigators were blinded to experimental groups (for example, analysis of all grip-strength measurements).

Study Approval. All animal protocols and experimental procedures for adenine diet in *FGFR4*$^{+/+}$ and *FGFR4*$^{-/-}$ mice, graded phosphate diets in *FGFR4*$^{+/+}$ and *FGFR4*$^{-/-}$ mice, low

764 phosphate diets in *COL4A3*$^{+/+}$ and *COL4A3*$^{-/-}$ mice and primary hepatocyte isolations from wild-
765 type C57BL/6J mice, were approved by the Institutional Animal Care and Use Committees
766 (IACUC) at the University of Alabama Birmingham School of Medicine. All animals were
767 maintained in a ventilated rodent-housing system with temperature-controlled environments (22–
768 23°C) with a 12-hour light/dark cycle and allowed *ad libitum* access to food and water. All
769 protocols adhered to the Guide for Care and Use of Laboratory Animals to minimize pain and
770 suffering. No animals were excluded from analysis.

771

772

773

774

775

776

777

778

779 **Acknowledgments**

780 BC designed and performed experiments, analyzed data and wrote the manuscript. KH, IC, CY,
781 DK, DW assisted with experiments. GJ measured liver and spleen iron concentrations in Alport
782 mice. OG, JBL, IBS, MH assisted with data analysis and interpretation. CF supervised project,
783 secured funding, assisted with data interpretation and edited manuscript. All authors discussed
784 results, read and contributed edits to manuscript and approved final version.

785 This study was supported by NIH grants F31-DK-117550 (BC), T90-DE-022736 (KH),
786 F31-DK-115074 (CY), K24-DK-116180 (OG), R01-DK-087727 (JLB), U01-DK-119950 (IBS),
787 K08-DK-111980 (MH), R01-HL-128714 and R01-HL-145528 (CF); and by grants from the
788 Deutsche Forschungsgemeinschaft (DK) and the National Science Foundation (IC). Furthermore,
789 CF was supported by the UAB-UCSD O'Brien Core Center for Acute Kidney Injury Research,
790 the AMC21 program of the Department of Medicine at UAB and the Tolwani Innovation Award
791 from the Division of Nephrology at UAB; JLB was supported by the Patricia and Scott Eston
792 Massachusetts General Hospital Research Scholar Award.

793

794

795

796

797

798

Competing Interests

The authors declare competing financial interests: CF has served as a consultant for Bayer and Calico Labs, and he is the founder and currently the CSO of a startup biotech company (Alpha Young LLC); OG has received honoraria and grant support from Akebia and Amgen, grant support from GSK, honoraria from Ardelyx, Reata, and AstraZeneca, and serves on the Data Monitoring Committee for QED; JLB has ownership interest in Ferrumax Pharmaceuticals and has been a consultant for Incyte Corporation, and Alnylam Pharmaceuticals.

809 **References**

810
811

812 Acevedo LM, López I, Peralta-Ramírez A, Pineda C, Chamizo VE, Rodríguez M, Aguilera-
813 Tejero E, Rivero J-LL. 2016. High-phosphorus diet maximizes and low-dose calcitriol
814 attenuates skeletal muscle changes in long-term uremic rats. *J Appl Physiol* 120:1059–1069.
815 doi:10.1152/japplphysiol.00957.2015

816 Agoro R, Montagna A, Goetz R, Aligbe O, Singh G, Coe LM, Mohammadi M, Rivella S, Sitara
817 D. 2018. Inhibition of fibroblast growth factor 23 (FGF23) signaling rescues renal anemia.
818 *Faseb J* 32:3752–3764. doi:10.1096/fj.201700667r

819 Amdur RL, Feldman HI, Gupta J, Yang W, Kanetsky P, Shlipak M, Rahman M, Lash JP,
820 Townsend RR, Ojo A, Roy-Chaudhury A, Go AS, Joffe M, He J, Balakrishnan VS, Kimmel
821 PL, Kusek JW, Raj DS, Investigators the CS. 2016. Inflammation and Progression of CKD:
822 The CRIC Study. *Clin J Am Soc Nephro* 11:1546–1556. doi:10.2215/cjn.13121215

823 Aschemeyer S, Qiao B, Stefanova D, Valore EV, Sek AC, Ruwe TA, Vieth KR, Jung G, Casu C,
824 Rivella S, Jormakka M, Mackenzie B, Ganz T, Nemeth E. 2018. Structure-function analysis
825 of ferroportin defines the binding site and an alternative mechanism of action of hepcidin.
826 *Blood* 131:899–910. doi:10.1182/blood-2017-05-786590

827 Avin KG, Vallejo JA, Chen NX, Wang K, Touchberry CD, Brotto M, Dallas SL, Moe SM,
828 Wacker MJ. 2018. Fibroblast growth factor 23 does not directly influence skeletal muscle cell
829 proliferation and differentiation or ex vivo muscle contractility. *Am J Physiol-endoc M*
830 315:E594–E604. doi:10.1152/ajpendo.00343.2017

831 Baquerizo A, Anselmo D, Shackleton C, Chen T-W, Cao C, Weaver M, Gornbein J,
832 Geevarghese S, Nissen N, Farmer D, Demetriou A, Busuttil RW. 2003. Phosphorus ans an
833 early predictive factor in patients with acute liver failure1. *Transplantation* 75:2007–2014.
834 doi:10.1097/01.tp.0000063219.21313.32

835 Billesbølle CB, Azumaya CM, Kretsch RC, Powers AS, Gonen S, Schneider S, Arvedson T,
836 Dror RO, Cheng Y, Manglik A. 2020. Structure of hepcidin-bound ferroportin reveals iron
837 homeostatic mechanisms. *Nature* 586:807–811. doi:10.1038/s41586-020-2668-z

838 Bon N, Couasnay G, Bourgine A, Sourice S, Beck-Cormier S, Guicheux J, Beck L. 2018.
839 Phosphate (Pi)-regulated heterodimerization of the high-affinity sodium-dependent Pi
840 transporters PiT1/Slc20a1 and PiT2/Slc20a2 underlies extracellular Pi sensing independently
841 of Pi uptake. *J Biol Chem* 293:2102–2114. doi:10.1074/jbc.m117.807339

842 Carrigan A, Klinger A, Choquette SS, Luzuriaga-McPherson A, Bell EK, Darnell B, Gutiérrez
843 OM. 2014. Contribution of Food Additives to Sodium and Phosphorus Content of Diets Rich
844 in Processed Foods. *J Renal Nutr* 24:13-19.e1. doi:10.1053/j.jrn.2013.09.003

845 Chang AR, Lazo M, Appel LJ, Gutiérrez OM, Grams ME. 2014. High dietary phosphorus intake
846 is associated with all-cause mortality: results from NHANES III. *Am J Clin Nutrition* 99:320–
847 327. doi:10.3945/ajcn.113.073148

848 Chavkin NW, Chia JJ, Crouthamel MH, Giachelli CM. 2015. Phosphate uptake-independent
849 signaling functions of the type III sodium-dependent phosphate transporter, PiT-1, in vascular
850 smooth muscle cells. *Exp Cell Res* 333:39–48. doi:10.1016/j.yexcr.2015.02.002

851 Chazot G, Lemoine S, Kocevar G, Kalbacher E, Sappey-Marinier D, Rouvière O, Juillard L.
852 2020. Intracellular Phosphate and ATP Depletion Measured by Magnetic Resonance
853 Spectroscopy in Patients Receiving Maintenance Hemodialysis. *J Am Soc Nephrol*
854 ASN.2020050716. doi:10.1681/asn.2020050716

855 Chen Y-Y, Kao T-W, Chou C-W, Wu C-J, Yang H-F, Lai C-H, Wu L-W, Chen W-L. 2018.
856 Exploring the Link between Serum Phosphate Levels and Low Muscle Strength, Dynapenia,
857 and Sarcopenia. *Sci Rep-uk* 8:3573. doi:10.1038/s41598-018-21784-1

858 Chung L-H, Liu S-T, Huang S-M, Salter DM, Lee H-S, Hsu Y-J. 2020. High phosphate induces
859 skeletal muscle atrophy and suppresses myogenic differentiation by increasing oxidative
860 stress and activating Nrf2 signaling. *Aging* 12:21446–21468. doi:10.18632/aging.103896

861 Clerin V, Saito H, Filipski KJ, Nguyen AH, Garren J, Kisucka J, Reyes M, Jüppner H. 2020.
862 Selective pharmacological inhibition of the sodium-dependent phosphate co-transporter
863 NPT2a promotes phosphate excretion. *J Clin Invest* 130:6510–6522. doi:10.1172/jci135665

864 Cosgrove D, Meehan DT, Grunkemeyer JA, Kornak JM, Sayers R, Hunter WJ, Samuelson GC.
865 1996. Collagen COL4A3 knockout: a mouse model for autosomal Alport syndrome. *Gene*
866 *Dev* 10:2981–2992. doi:10.1101/gad.10.23.2981

867 Czaya B, Faul C. 2019a. The Role of Fibroblast Growth Factor 23 in Inflammation and Anemia.
868 *Int J Mol Sci* 20:4195. doi:10.3390/ijms20174195

869 Czaya B, Faul C. 2019b. FGF23 and inflammation—a vicious coalition in CKD. *Kidney Int*
870 96:813–815. doi:10.1016/j.kint.2019.05.018

871 Erem S, Razzaque MS. 2018. Dietary phosphate toxicity: an emerging global health concern.
872 *Histochem Cell Biol* 150:711–719. doi:10.1007/s00418-018-1711-8

873 Falzacappa MVV, Spasic MV, Kessler R, Stolte J, Hentze MW, Muckenthaler MU. 2007.
874 STAT3 mediates hepatic hepcidin expression and its inflammatory stimulation. *Blood*
875 109:353–358. doi:10.1182/blood-2006-07-033969

Farrow EG, Imel EA, White KE. 2011. Hyperphosphatemic familial tumoral calcinosis (FGF23, GALNT3 and αKlotho). *Best Pract Res Clin Rheumatology* 25:735–747. doi:10.1016/j.berh.2011.10.020

Faul C, Amaral AP, Oskouei B, Hu M-C, Sloan A, Isakova T, Gutiérrez OM, Aguillon-Prada R, Lincoln J, Hare JM, Mundel P, Morales A, Scialla J, Fischer M, Soliman EZ, Chen J, Go AS, Rosas SE, Nessel L, Townsend RR, Feldman HI, Sutton MStJ, Ojo A, Gadegbeku C, Marco GSD, Reuter S, Kentrup D, Tiemann K, Brand M, Hill JA, Moe OW, Kuro-o M, Kusek JW, Keane MG, Wolf M. 2011. FGF23 induces left ventricular hypertrophy. *J Clin Invest* 121:4393–4408. doi:10.1172/jci46122

Forand A, Koumakis E, Rousseau A, Sassier Y, Journe C, Merlin J-F, Leroy C, Boitez V, Codogno P, Friedlander G, Cohen I. 2016. Disruption of the Phosphate Transporter Pit1 in Hepatocytes Improves Glucose Metabolism and Insulin Signaling by Modulating the USP7/IRS1 Interaction. *Cell Reports* 16:2736–2748. doi:10.1016/j.celrep.2016.08.012

Francis C, Courbon G, Gerber C, Neuburg S, Wang X, Dussold C, Capella M, Qi L, Isakova T, Mehta R, Martin A, Wolf M, David V. 2019. Ferric citrate reduces fibroblast growth factor 23 levels and improves renal and cardiac function in a mouse model of chronic kidney disease. *Kidney Int* 96:1346–1358. doi:10.1016/j.kint.2019.07.026

Fukumoto S, Yamashita T. 2007. FGF23 is a hormone-regulating phosphate metabolism—Unique biological characteristics of FGF23. *Bone* 40:1190–1195. doi:10.1016/j.bone.2006.12.062

Ganz T, Nemeth E. 2012. Hepcidin and iron homeostasis. *Biochimica Et Biophysica Acta Bba - Mol Cell Res* 1823:1434–1443. doi:10.1016/j.bbamcr.2012.01.014

Grabner A, Amaral AP, Schramm K, Singh S, Sloan A, Yanucil C, Li J, Shehadeh LA, Hare JM, David V, Martin A, Fornoni A, Marco GSD, Kentrup D, Reuter S, Mayer AB, Pavenstädt H, Stypmann J, Kuhn C, Hille S, Frey N, Leifheit-Nestler M, Richter B, Haffner D, Abraham R, Bange J, Sperl B, Ullrich A, Brand M, Wolf M, Faul C. 2015. Activation of Cardiac Fibroblast Growth Factor Receptor 4 Causes Left Ventricular Hypertrophy. *Cell Metab* 22:1020–32. doi:10.1016/j.cmet.2015.09.002

Gutiérrez OM, Anderson C, Isakova T, Scialla J, Negrea L, Anderson AH, Bellovich K, Chen J, Robinson N, Ojo A, Lash J, Feldman HI, Wolf M, Group on behalf of the CS. 2010. Low Socioeconomic Status Associates with Higher Serum Phosphate Irrespective of Race. *J Am Soc Nephrol* 21:1953–1960. doi:10.1681/asn.2010020221

Gutiérrez OM, Wolf M. 2010. Dietary Phosphorus Restriction in Advanced Chronic Kidney Disease: Merits, Challenges, and Emerging Strategies. *Semin Dialysis* 23:401–406. doi:10.1111/j.1525-139x.2010.00750.x

911 Han X, Cai C, Xiao Z, Quarles LD. 2020. FGF23 induced left ventricular hypertrophy mediated
912 by FGFR4 signaling in the myocardium is attenuated by soluble Klotho in mice. *J Mol Cell*
913 *Cardiol* 138:66–74. doi:10.1016/j.yjmcc.2019.11.149

914 Haut LL, Alfrey AC, Guggenheim S, Buddington B, Schrier N. 1980. Renal toxicity of
915 phosphate in rats. *Kidney Int* 17:722–731. doi:10.1038/ki.1980.85

916 Hoshino J, Muenz D, Zee J, Sukul N, Speyer E, Guedes M, Lopes AA, Asahi K, Haalen H van,
917 James G, Dhalwani N, Pecoits-Filho R, Bieber B, Robinson BM, Pisoni RL, Investigators
918 Ckd, Lopes A, Pecoits-Filho R, Combe C, Jacquelinet C, Massy Z, Stengel B, Duttlinger J,
919 Fliser D, Lonnemann G, Reichel H, Wada T, Yamagata K, Pisoni R, Robinson B, Silva VC
920 da, Sesso R, Speyer E, Asahi K, Hoshino J, Narita I, Perlman R, Port F, Sukul N, Wong M,
921 Young E, Zee J. 2020. Associations of Hemoglobin Levels With Health-Related Quality of
922 Life, Physical Activity, and Clinical Outcomes in Persons With Stage 3-5 Nondialysis CKD.
923 *J Renal Nutr* 30:404–414. doi:10.1053/j.jrn.2019.11.003

924 Isakova T, Gutierrez O, Shah A, Castaldo L, Holmes J, Lee H, Wolf M. 2008. Postprandial
925 Mineral Metabolism and Secondary Hyperparathyroidism in Early CKD. *J Am Soc Nephrol*
926 19:615–623. doi:10.1681/asn.2007060673

927 Isakova T, Gutiérrez OM, Chang Y, Shah A, Tamez H, Smith K, Thadhani R, Wolf M. 2009.
928 Phosphorus Binders and Survival on Hemodialysis. *J Am Soc Nephrol* 20:388–396.
929 doi:10.1681/asn.2008060609

930 Isakova T, Wahl P, Vargas GS, Gutiérrez OM, Scialla J, Xie H, Appleby D, Nessel L, Bellovich
931 K, Chen J, Hamm L, Gadegbeku C, Horwitz E, Townsend RR, Anderson CAM, Lash JP, Hsu
932 C, Leonard MB, Wolf M, Group on behalf of the CRIC (CRIC) S. 2011. Fibroblast growth
933 factor 23 is elevated before parathyroid hormone and phosphate in chronic kidney disease.
934 *Kidney Int* 79:1370–1378. doi:10.1038/ki.2011.47

935 Kanamori Y, Murakami M, Sugiyama M, Hashimoto O, Matsui T, Funaba M. 2017. Interleukin-
936 1β (IL-1β) transcriptionally activates hepcidin by inducing CCAAT enhancer-binding protein
937 δ (C/EBPδ) expression in hepatocytes. *J Biol Chem* 292:10275–10287.
938 doi:10.1074/jbc.m116.770974

939 Komaba H, Fukagawa M. 2016. Phosphate—a poison for humans? *Kidney Int* 90:753–763.
940 doi:10.1016/j.kint.2016.03.039

941 Koumakis E, Millet-Botti J, Benna JE, Leroy C, Boitez V, Codogno P, Friedlander G, Forand A.
942 2019. Novel function of PiT1/SLC20A1 in LPS-related inflammation and wound healing. *Sci*
943 *Rep-uk* 9:1808. doi:10.1038/s41598-018-37551-1

944 Kovesdy CP, Kopple JD, Kalantar-Zadeh K. 2013. Management of protein-energy wasting in
945 non-dialysis-dependent chronic kidney disease: reconciling low protein intake with nutritional
946 therapy. *Am J Clin Nutrition* 97:1163–1177. doi:10.3945/ajcn.112.036418

947 Lederer E, Miyamoto K. 2012. Clinical Consequences of Mutations in Sodium Phosphate
948 Cotransporters. *Clin J Am Soc Nephro* 7:1179–1187. doi:10.2215/cjn.09090911

949 Leifheit-Nestler M, Grabner A, Hermann L, Richter B, Schmitz K, Fischer D-C, Yanucil C, Faul
950 C, Haffner D. 2017. Vitamin D treatment attenuates cardiac FGF23/FGFR4 signaling and
951 hypertrophy in uremic rats. *Nephrol Dial Transpl* 32:1493–1503. doi:10.1093/ndt/gfw454

952 Li W, Moylan JS, Chambers MA, Smith J, Reid MB. 2009. Interleukin-1 stimulates catabolism
953 in C2C12 myotubes. *Am J Physiol-cell Ph* 297:C706–C714. doi:10.1152/ajpcell.00626.2008

954 Mehta R, Cai X, Hodakowski A, Lee J, Leonard M, Ricardo A, Chen J, Hamm L, Sondheimer J,
955 Dobre M, David V, Yang W, Go A, Kusek JW, Feldman H, Wolf M, Isakova T, Investigators
956 CS. 2017. Fibroblast Growth Factor 23 and Anemia in the Chronic Renal Insufficiency
957 Cohort Study. *Clin J Am Soc Nephro* 12:1795–1803. doi:10.2215/cjn.03950417

958 Mendoza JM, Isakova T, Cai X, Bayes LY, Faul C, Scialla JJ, Lash JP, Chen J, He J,
959 Navaneethan S, Negrea L, Rosas SE, Kretzler M, Nessel L, Xie D, Anderson AH, Raj DS,
960 Wolf M, Investigators CS, Appel LJ, Feldman HI, Go AS, He J, Kusek JW, Lash JP, Ojo A,
961 Townsend RR. 2017. Inflammation and elevated levels of fibroblast growth factor 23 are
962 independent risk factors for death in chronic kidney disease. *Kidney Int* 91:711–719.
963 doi:10.1016/j.kint.2016.10.021

964 Morishita K, Shirai A, Kubota M, Katakura Y, Nabeshima Y, Takeshige K, Kamiya T. 2001.
965 The Progression of Aging in Klotho Mutant Mice Can Be Modified by Dietary Phosphorus
966 and Zinc. *J Nutrition* 131:3182–3188. doi:10.1093/jn/131.12.3182

967 Nakao M, Yamamoto H, Nakahashi O, Ikeda S, Abe K, Masuda M, Ishiguro M, Iwano M,
968 Takeda E, Taketani Y. 2015. Dietary phosphate supplementation delays the onset of iron
969 deficiency anemia and affects iron status in rats. *Nutr Res* 35:1016–1024.
970 doi:10.1016/j.nutres.2015.09.001

971 Navarro-González JF, Mora-Fernández C, Muros M, Herrera H, García J. 2009. Mineral
972 Metabolism and Inflammation in Chronic Kidney Disease Patients: A Cross-Sectional Study.
973 *Clin J Am Soc Nephro* 4:1646–1654. doi:10.2215/cjn.02420409

974 Nemeth E, Rivera S, Gabayan V, Keller C, Taudorf S, Pedersen BK, Ganz T. 2004a. IL-6
975 mediates hypoferremia of inflammation by inducing the synthesis of the iron regulatory
976 hormone hepcidin. *J Clin Invest* 113:1271–1276. doi:10.1172/jci20945

977 Nemeth E, Tuttle MS, Powelson J, Vaughn MB, Donovan A, Ward DM, Ganz T, Kaplan J.
978 2004b. Hepcidin Regulates Cellular Iron Efflux by Binding to Ferroportin and Inducing Its
979 Internalization. *Science* 306:2090–2093. doi:10.1126/science.1104742

980 Noonan ML, Clinkenbeard EL, Ni P, Swallow EA, Tippen SP, Agoro R, Allen MR, White KE.
981 2020. Erythropoietin and a hypoxia-inducible factor prolyl hydroxylase inhibitor (HIF-PHDi)

lowers FGF23 in a model of chronic kidney disease (CKD). *Physiological Reports* 8:e14434. doi:10.14814/phy2.14434

Pierce JW, Schoenleber R, Jesmok G, Best J, Moore SA, Collins T, Gerritsen ME. 1997. Novel Inhibitors of Cytokine-induced IκBα Phosphorylation and Endothelial Cell Adhesion Molecule Expression Show Anti-inflammatory Effects in Vivo *. *J Biol Chem* 272:21096–21103. doi:10.1074/jbc.272.34.21096

Raj DSC, Moseley P, Dominic EA, Onime A, Tzamaloukas AH, Boyd A, Shah VO, Glew R, Wolfe R, Ferrando A. 2008. Interleukin-6 modulates hepatic and muscle protein synthesis during hemodialysis. *Kidney Int* 73:1054–1061. doi:10.1038/ki.2008.21

Ramnitz MS, Gourh P, Goldbach-Mansky R, Wodajo F, Ichikawa S, Econs MJ, White KE, Molinolo A, Chen MY, Heller T, Rivero JD, Seo-Mayer P, Arabshahi B, Jackson MB, Hatab S, McCarthy E, Guthrie LC, Brillante BA, Gafni RI, Collins MT. 2016. Phenotypic and Genotypic Characterization and Treatment of a Cohort With Familial Tumoral Calcinosis/Hyperostosis-Hyperphosphatemia Syndrome. *J Bone Miner Res* 31:1845–1854. doi:10.1002/jbmr.2870

Rodríguez-Ortiz ME, Díaz-Tocados JM, Muñoz-Castañeda JR, Herencia C, Pineda C, Martínez-Moreno JM, Oca AM de, López-Baltanás R, Alcalá-Díaz J, Ortiz A, Aguilera-Tejero E, Felsenfeld A, Rodríguez M, Almadén Y. 2020. Inflammation both increases and causes resistance to FGF23 in normal and uremic rats. *Clin Sci* 134:15–32. doi:10.1042/cs20190779

Schaap LA, Pluijm SMF, Deeg DJH, Visser M. 2006. Inflammatory Markers and Loss of Muscle Mass (Sarcopenia) and Strength. *Am J Medicine* 119:526.e9-526.e17. doi:10.1016/j.amjmed.2005.10.049

Scialla JJ, Wolf M. 2014. Roles of phosphate and fibroblast growth factor 23 in cardiovascular disease. *Nat Rev Nephrol* 10:268–278. doi:10.1038/nrneph.2014.49

Shiizaki K, Tsubouchi A, Miura Y, Seo K, Kuchimaru T, Hayashi H, Iwazu Y, Miura M, Battulga B, Ohno N, Hara T, Kunishige R, Masutani M, Negishi K, Kario K, Kotani K, Yamada T, Nagata D, Komuro I, Itoh H, Kurosu H, Murata M, Kuro-o M. 2021. Calcium phosphate microcrystals in the renal tubular fluid accelerate chronic kidney disease progression. *J Clin Invest* 131. doi:10.1172/jci145693

Singh S, Grabner A, Yanucil C, Schramm K, Czaya B, Krick S, Czaja MJ, Bartz R, Abraham R, Marco GSD, Brand M, Wolf M, Faul C. 2016. Fibroblast growth factor 23 directly targets hepatocytes to promote inflammation in chronic kidney disease. *Kidney Int* 90:985–996. doi:10.1016/j.kint.2016.05.019

Stenvinkel P, Carrero JJ, Walden F von, Ikizler TA, Nader GA. 2016. Muscle wasting in end-stage renal disease promulgates premature death: established, emerging and potential novel treatment strategies. *Nephrol Dial Transpl* 31:1070–1077. doi:10.1093/ndt/gfv122

1018 Sugihara K, Masuda M, Nakao M, Abuduli M, Imi Y, Oda N, Okahisa T, Yamamoto H, Takeda
1019 E, Taketani Y. 2017. Dietary phosphate exacerbates intestinal inflammation in experimental
1020 colitis. *J Clin Biochem Nutr* 61:16–117. doi:10.3164/jcbn.16-117

1021 Takashi Y, Kosako H, Sawatsubashi S, Kinoshita Y, Ito N, Tsoumpra MK, Nangaku M, Abe M,
1022 Matsuhisa M, Kato S, Matsumoto T, Fukumoto S. 2019. Activation of unliganded FGF
1023 receptor by extracellular phosphate potentiates proteolytic protection of FGF23 by its O-
1024 glycosylation. *Proc National Acad Sci* 116:201815166. doi:10.1073/pnas.1815166116

1025 Taylor A, Yanucil C, Musgrove J, Shi M, Ide S, Souma T, Faul C, Wolf M, Grabner A. 2019.
1026 FGFR4 does not contribute to progression of chronic kidney disease. *Sci Rep-uk* 9:14023.
1027 doi:10.1038/s41598-019-50669-0

1028 Thomas L, Xue J, Murali SK, Fenton RA, Rieg JAD, Rieg T. 2019. Pharmacological Npt2a
1029 Inhibition Causes Phosphaturia and Reduces Plasma Phosphate in Mice with Normal and
1030 Reduced Kidney Function. *J Am Soc Nephrol* 30:2128–2139. doi:10.1681/asn.2018121250

1031 Toussaint ND, Pedagogos E, Lioufas NM, Elder GJ, Pascoe EM, Badve SV, Valks A, Block GA,
1032 Boudville N, Cameron JD, Campbell KL, Chen SSM, Faull RJ, Holt SG, Jackson D, Jardine
1033 MJ, Johnson DW, Kerr PG, Lau KK, Hooi L-S, Narayan O, Perkovic V, Polkinghorne KR,
1034 Pollock CA, Reidlinger D, Robison L, Smith ER, Walker RJ, Wang AYM, Hawley CM,
1035 Investigators I-CT. 2020. A Randomized Trial on the Effect of Phosphate Reduction on
1036 Vascular End Points in CKD (IMPROVE-CKD). *J Am Soc Nephrol* 31:2653–2666.
1037 doi:10.1681/asn.2020040411

1038 Tran L, Batech M, Rhee CM, Streja E, Kalantar-Zadeh K, Jacobsen SJ, Sim JJ. 2016. Serum
1039 phosphorus and association with anemia among a large diverse population with and without
1040 chronic kidney disease. *Nephrol Dial Transpl* 31:636–645. doi:10.1093/ndt/gfv297

1041 Turner ME, Lansing AP, Jeronimo PS, Lee LH, Svajger BA, Zelt JG, Forster CM, Petkovich
1042 MP, Holden RM, Adams MA. 2020. Vascular calcification has a role in acute non-renal
1043 phosphate clearance. *Biorxiv* 2020.07.29.225532. doi:10.1101/2020.07.29.225532

1044 Ugrica M, Bettoni C, Bourgeois S, Daryadel A, Pastor-Arroyo E-M, Gehring N, Hernando N,
1045 Wagner CA, Rubio-Aliaga I. 2021. A chronic high phosphate intake in mice is detrimental for
1046 bone health without major renal alterations. *Nephrol Dial Transpl* 36:1183–1191.
1047 doi:10.1093/ndt/gfab015

1048 Verzola D, Barisione C, Picciotto D, Garibotto G, Koppe L. 2018. Emerging role of myostatin
1049 and its inhibition in the setting of chronic kidney disease. *Kidney Int* 95:506–517.
1050 doi:10.1016/j.kint.2018.10.010

1051 Verzola D, Bonanni A, Sofia A, Montecucco F, D'Amato E, Cademartori V, Parodi EL, Viazzi
1052 F, Venturelli C, Brunori G, Garibotto G. 2016. Toll-like receptor 4 signalling mediates
1053 inflammation in skeletal muscle of patients with chronic kidney disease. *J Cachexia*
1054 *Sarcopenia Muscle* 8:131–144. doi:10.1002/jcsm.12129

1055 Villa-Bellosta R, Bogaert YE, Levi M, Sorribas V. 2007. Characterization of Phosphate
1056 Transport in Rat Vascular Smooth Muscle Cells. *Arteriosclerosis Thrombosis Vasc Biology*
1057 27:1030–1036. doi:10.1161/atvbaha.106.132266

1058 Villa-Bellosta R, Sorribas V. 2009. Phosphonoformic Acid Prevents Vascular Smooth Muscle
1059 Cell Calcification by Inhibiting Calcium-Phosphate Deposition. *Arteriosclerosis Thrombosis*
1060 *Vasc Biology* 29:761–766. doi:10.1161/atvbaha.108.183384

1061 Voelkl J, Tuffaha R, Luong TTD, Zickler D, Masyout J, Feger M, Verheyen N, Blaschke F,
1062 Kuro-o M, Tomaschitz A, Pilz S, Pasch A, Eckardt K-U, Scherberich JE, Lang F, Pieske B,
1063 Alesutan I. 2018. Zinc Inhibits Phosphate-Induced Vascular Calcification through TNFAIP3-
1064 Mediated Suppression of NF-κB. *J Am Soc Nephrol* 29:1636–1648.
1065 doi:10.1681/asn.2017050492

1066 Wang XH, Mitch WE. 2014. Mechanisms of muscle wasting in chronic kidney disease. *Nat Rev*
1067 *Nephrol* 10:504–516. doi:10.1038/nrneph.2014.112

1068 Weinstein M, Xu X, Ohyama K, Deng CX. 1998. FGFR-3 and FGFR-4 function cooperatively to
1069 direct alveogenesis in the murine lung. *Dev Camb Engl* 125:3615–23.

1070 White KE, Carn G, Lorenz-Depiereux B, Benet-Pages A, Strom TM, Econs MJ. 2001.
1071 Autosomal-dominant hypophosphatemic rickets (ADHR) mutations stabilize FGF-23. *Kidney*
1072 *Int* 60:2079–2086. doi:10.1046/j.1523-1755.2001.00064.x

1073 Wojcicki JM. 2013. Hyperphosphatemia is associated with anemia in adults without chronic
1074 kidney disease: results from the National Health and Nutrition Examination Survey
1075 (NHANES): 2005–2010. *Bmc Nephrol* 14:178. doi:10.1186/1471-2369-14-178

1076 Wolf M. 2012. Update on fibroblast growth factor 23 in chronic kidney disease. *Kidney Int*
1077 82:737–747. doi:10.1038/ki.2012.176

1078 Xiao Z, King G, Mancarella S, Munkhsaikhan U, Cao L, Cai C, Quarles LD. 2019. FGF23
1079 expression is stimulated in transgenic α-Klotho longevity mouse model. *Jci Insight*
1080 4:e132820. doi:10.1172/jci.insight.132820

1081 Yamada S, Tokumoto M, Tatsumoto N, Taniguchi M, Noguchi H, Nakano T, Masutani K,
1082 Ooboshi H, Tsuruya K, Kitazono T. 2014. Phosphate overload directly induces systemic
1083 inflammation and malnutrition as well as vascular calcification in uremia. *Am J Physiol-renal*
1084 306:F1418–F1428. doi:10.1152/ajprenal.00633.2013

1085 Zelt JG, Svajger BA, Quinn K, Turner ME, Laverty KJ, Shum B, Holden RM, Adams MA.
1086 2019. Acute Tissue Mineral Deposition in Response to a Phosphate Pulse in Experimental
1087 CKD. *J Bone Miner Res* 34:270–281. doi:10.1002/jbmr.3572

Zhang L, Pan J, Dong Yanjun, Tweardy DJ, Dong Yanlan, Garibotto G, Mitch WE. 2013. Stat3 Activation Links a C/EBPδ to Myostatin Pathway to Stimulate Loss of Muscle Mass. *Cell Metab* 18:368–379. doi:10.1016/j.cmet.2013.07.012

Zhang L, Rajan V, Lin E, Hu Z, Han HQ, Zhou X, Song Y, Min H, Wang X, Du J, Mitch WE. 2011. Pharmacological inhibition of myostatin suppresses systemic inflammation and muscle atrophy in mice with chronic kidney disease. *Faseb J* 25:1653–1663. doi:10.1096/fj.10-176917

Zhao M-M, Xu M-J, Cai Y, Zhao G, Guan Y, Kong W, Tang C, Wang X. 2011. Mitochondrial reactive oxygen species promote p65 nuclear translocation mediating high-phosphate-induced vascular calcification in vitro and in vivo. *Kidney Int* 79:1071–1079. doi:10.1038/ki.2011.18

Zhou Z, Xu M-J, Gao B. 2016. Hepatocytes: a key cell type for innate immunity. *Cell Mol Immunol* 13:301–315. doi:10.1038/cmi.2015.97

Figures and Figure Legends

Figure 1

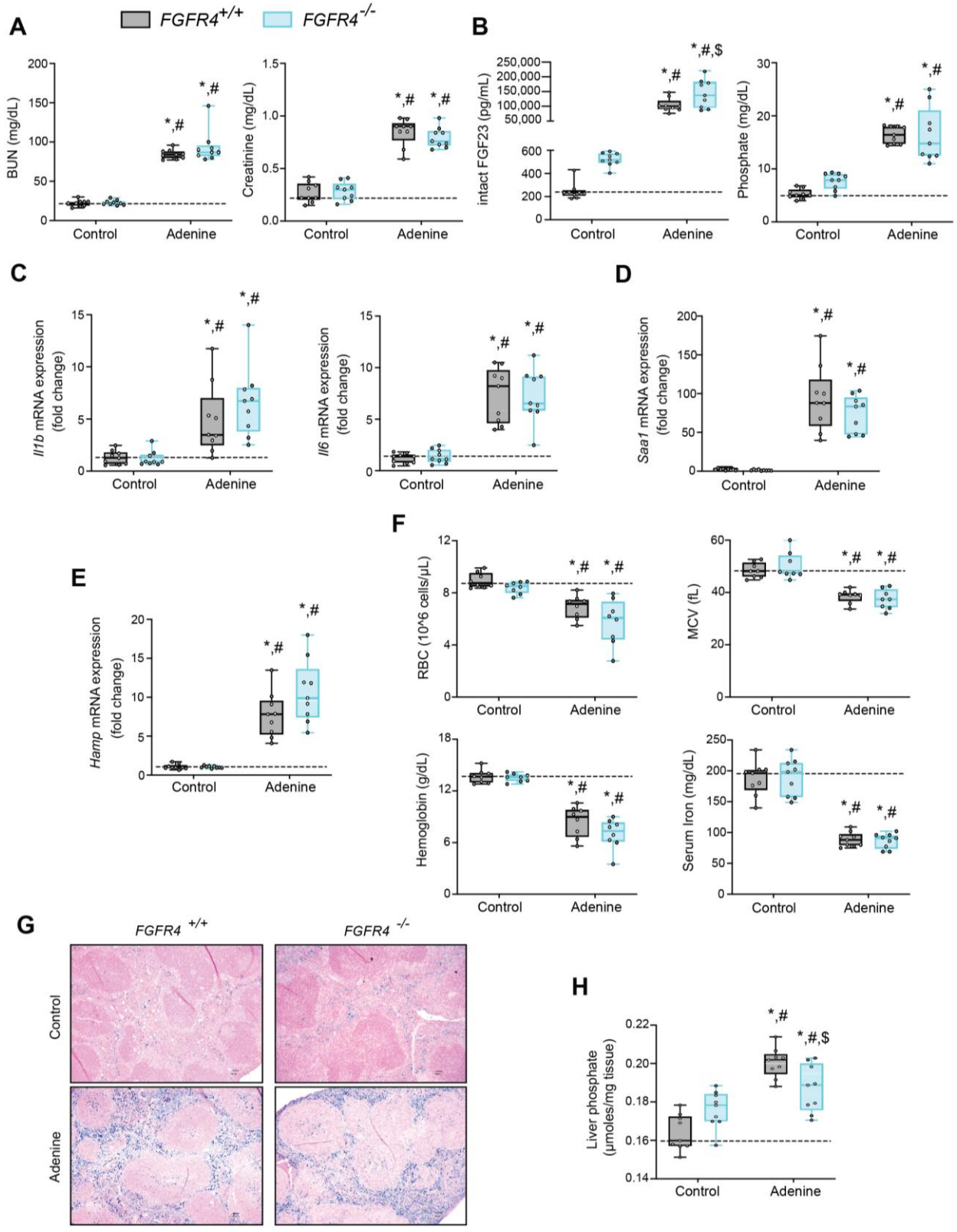

Figure 1. FGF23-FGFR4 signaling does not contribute to functional iron deficiency in adenine-induced CKD.

(**A-B**) Blood urea nitrogen (BUN), serum creatinine (A), serum FGF23 and serum phosphate (Pi) levels (B). (**C-E**) Quantitative PCR (qPCR) analysis of *Il1b*, *Il6*, *Saa1* (C-D) and *Hamp* (E) expression levels in liver tissue. (**F**) Complete blood count (CBC) analysis. (**G**) Representative gross pathology of perls' prussian blue-stained spleen sections (scale bar, 50 μm). (**H**) Liver Pi levels. All values are mean ± SEM (n = 8–9 mice/group; *p ≤ 0.05 vs. $FGFR4^{+/+}$ + control diet, #p ≤ 0.05 vs. $FGFR4^{-/-}$ + control diet, $p ≤ 0.05 vs. $FGFR4^{+/+}$ + adenine diet) where statistical analyses were calculated by two-way ANOVA followed by Tukey's multiple comparison post-hoc test. Dotted lines indicate median $FGFR4^{+/+}$ + control diet measurements.

1133 **Figure 2**

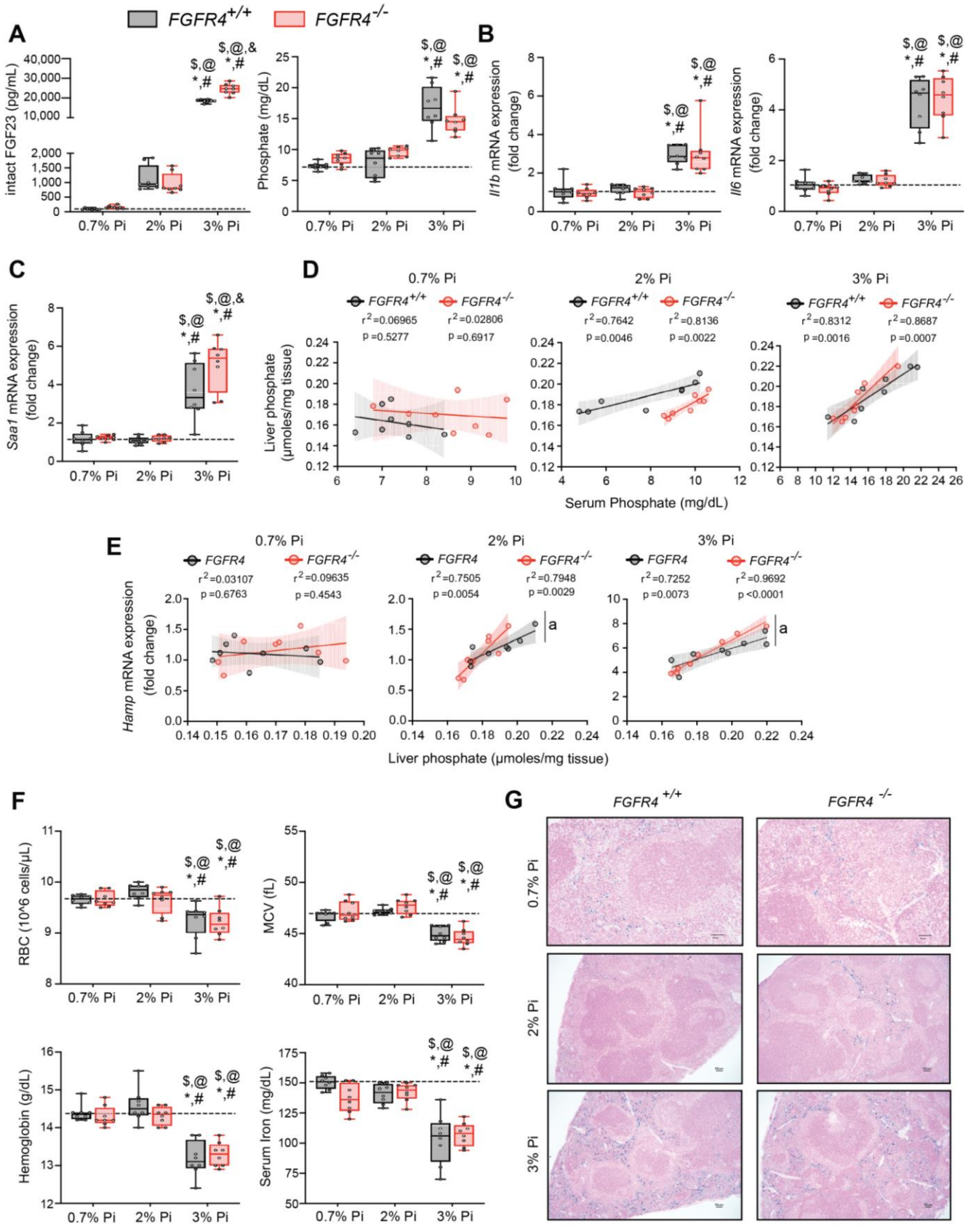

Figure 2. FGF23-FGFR4 signaling does not contribute to hypoferremia following dietary Pi overload.

(**A**) Serum FGF23 and serum Pi levels. (**B-C**) qPCR analysis of *Il1b*, *Il6* and *Saa1* expression levels in liver tissue. (**D**) Scatter plots showing correlations between liver Pi and serum Pi levels. (**E**) Scatter plots showing correlations between liver *Hamp* expression and liver Pi levels (a= slopes are significantly different from each other). (**F**) CBC analysis. (**G**) Representative gross pathology of perls' prussian blue-stained spleen sections (scale bar, 50 μm). All values are mean ± SEM (n = 8 mice/group; *p ≤ 0.05 vs. $FGFR4^{+/+}$ + 0.7% Pi diet, #p ≤ 0.05 vs. $FGFR4^{-/-}$ + 0.7% Pi diet, $p ≤ 0.05 vs. $FGFR4^{+/+}$ + 2% Pi diet, @p ≤ 0.05 vs. $FGFR4^{-/-}$ + 2% Pi diet, &p ≤ 0.05 vs. $FGFR4^{+/+}$ + 3% Pi diet) where statistical analyses were calculated by two-way ANOVA followed by Tukey's multiple comparison post-hoc test. Dotted lines indicate median $FGFR4^{+/+}$ + 0.7% Pi diet measurements. Scatter plot shadows indicate 95% confidence interval.

1154 **Figure 3**

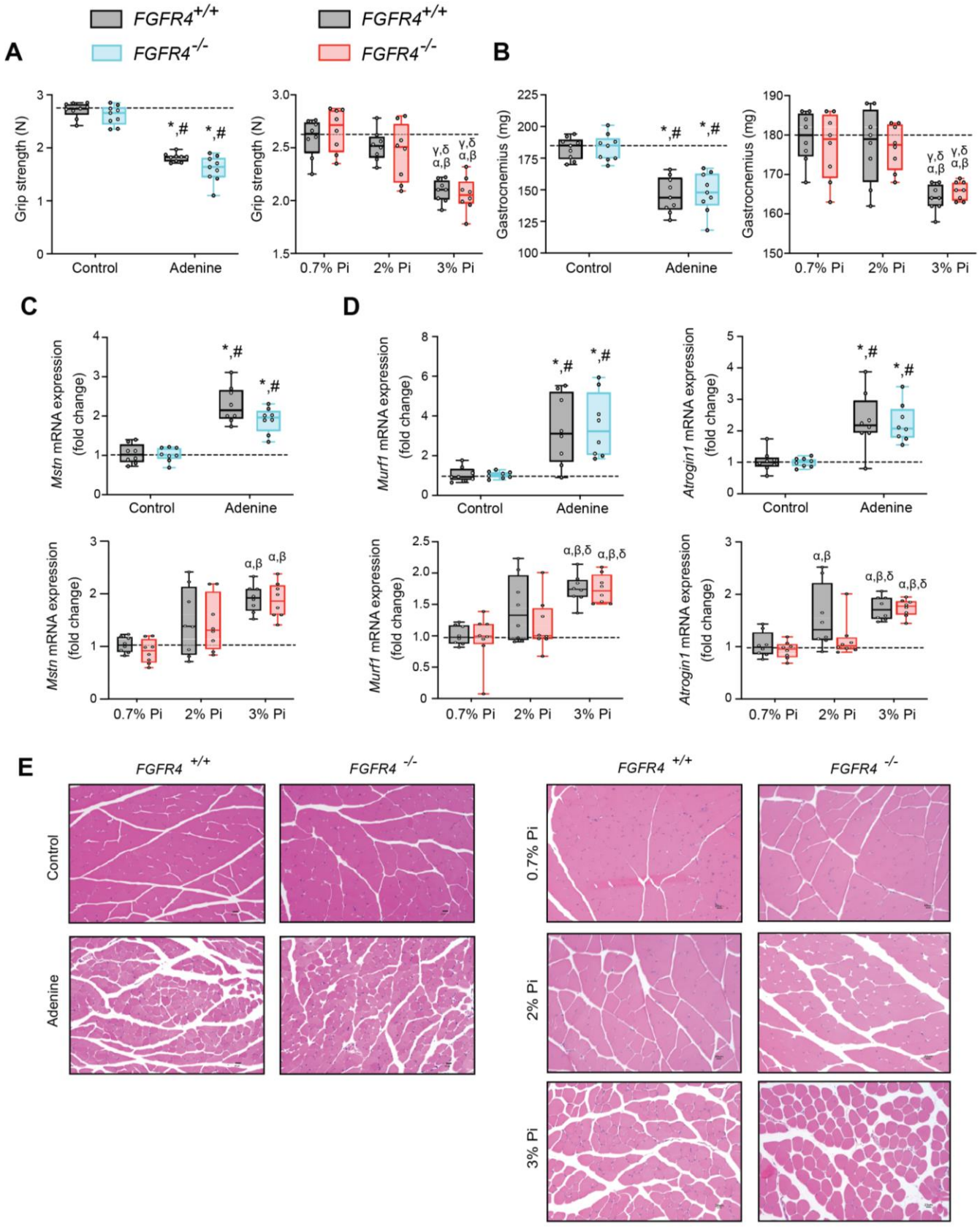

Figure 3. Mouse models of hyperphosphatemia exhibit signs of skeletal muscle wasting which are independent of FGF23-FGFR4 signaling.

(**A**) Grip strength. (**B**) Gastrocnemius weight. (**C-D**) qPCR analysis of *Mstn* (C), *Murf1* and *Atrogin1* (D) expression levels in gastrocnemius tissue. (**E**) Representative gross pathology of H&E-stained gastrocnemius sections (scale bar, 20 μm). All values are mean ± SEM ((n = 8–9 mice/group; *$p \leq 0.05$ vs. $FGFR4^{+/+}$ + control diet, #$p \leq 0.05$ vs. $FGFR4^{-/-}$ + control diet); (n = 8 mice/group; $^{\alpha}p \leq 0.05$ vs. $FGFR4^{+/+}$ + 0.7% Pi diet, $^{\beta}p \leq 0.05$ vs. $FGFR4^{-/-}$ + 0.7% Pi diet, $^{\gamma}p \leq 0.05$ vs. $FGFR4^{+/+}$ + 2% Pi diet, $^{\delta}p \leq 0.05$ vs. $FGFR4^{-/-}$ + 2% Pi diet)) where statistical analyses were calculated by two-way ANOVA followed by Tukey's multiple comparison post-hoc test. Dotted lines indicate median $FGFR4^{+/+}$ + control diet or $FGFR4^{+/+}$ + 0.7% Pi diet measurements.

1166 **Figure 4**

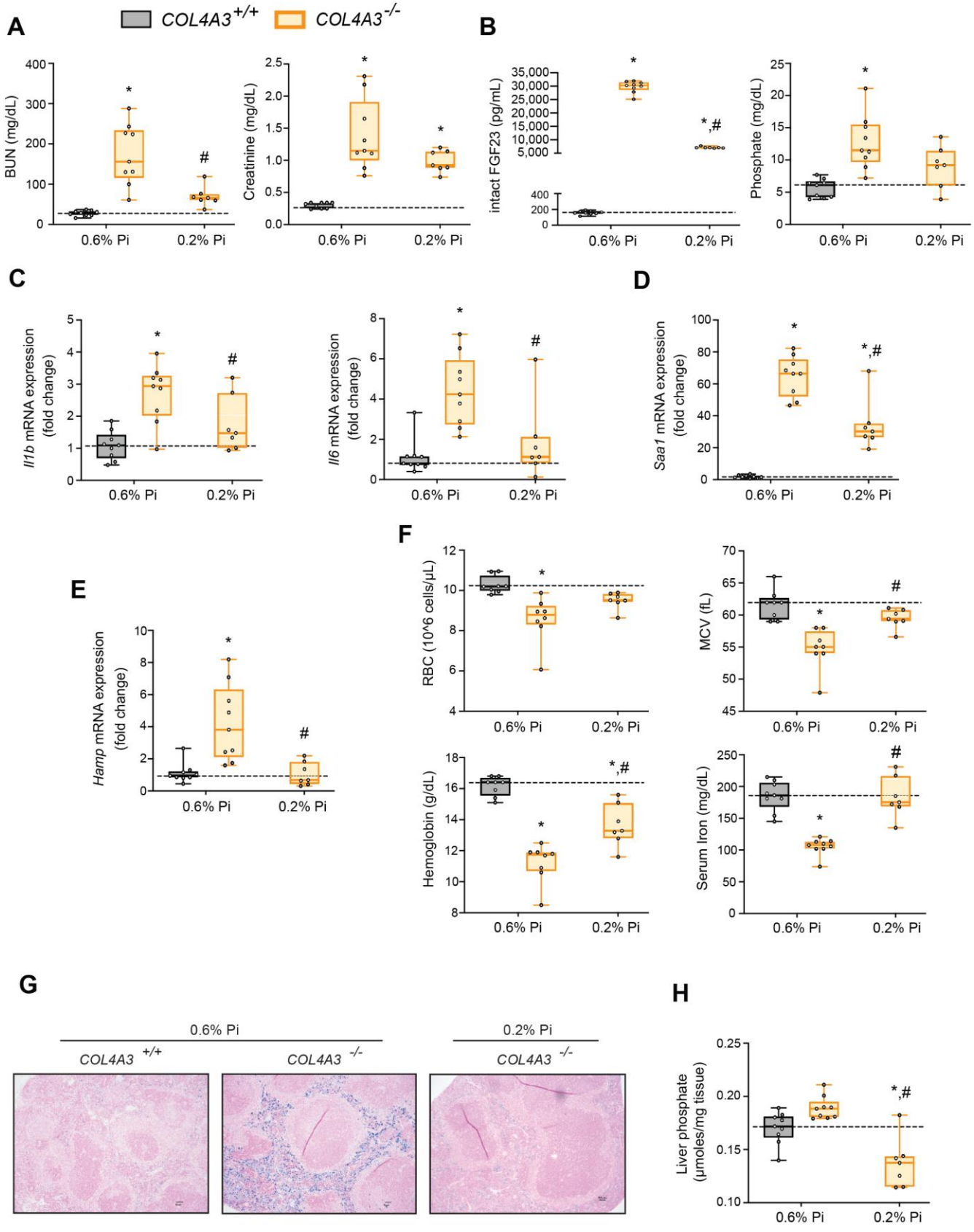

Figure 4. Low Pi feeding limits functional iron deficiency in *COL4A3*$^{-/-}$ (Alport syndrome) mice.

(**A-B**) BUN, serum creatinine (A), serum FGF23 and serum Pi levels (B). (**C-E**) qPCR analysis of *Il1b*, *Il6* and *Saa1* (C-D) and *Hamp* (E) expression levels in liver tissue. (**F**) CBC analysis. (**G**) Representative gross pathology of perls' prussian blue-stained spleen sections (scale bar, 50 μm). (**H**) Liver Pi levels. All values are mean ± SEM (n = 7-9 mice/group; *$p \leq 0.05$ vs. COL4A3$^{+/+}$ + 0.6% Pi diet, #$p \leq 0.05$ vs. COL4A3$^{-/-}$ + 0.6% Pi diet) where statistical analyses were calculated by two-way ANOVA followed by Tukey's multiple comparison post-hoc test. Dotted lines indicate median *COL4A3*$^{+/+}$ + 0.6% Pi diet measurements.

1186 **Figure 5**

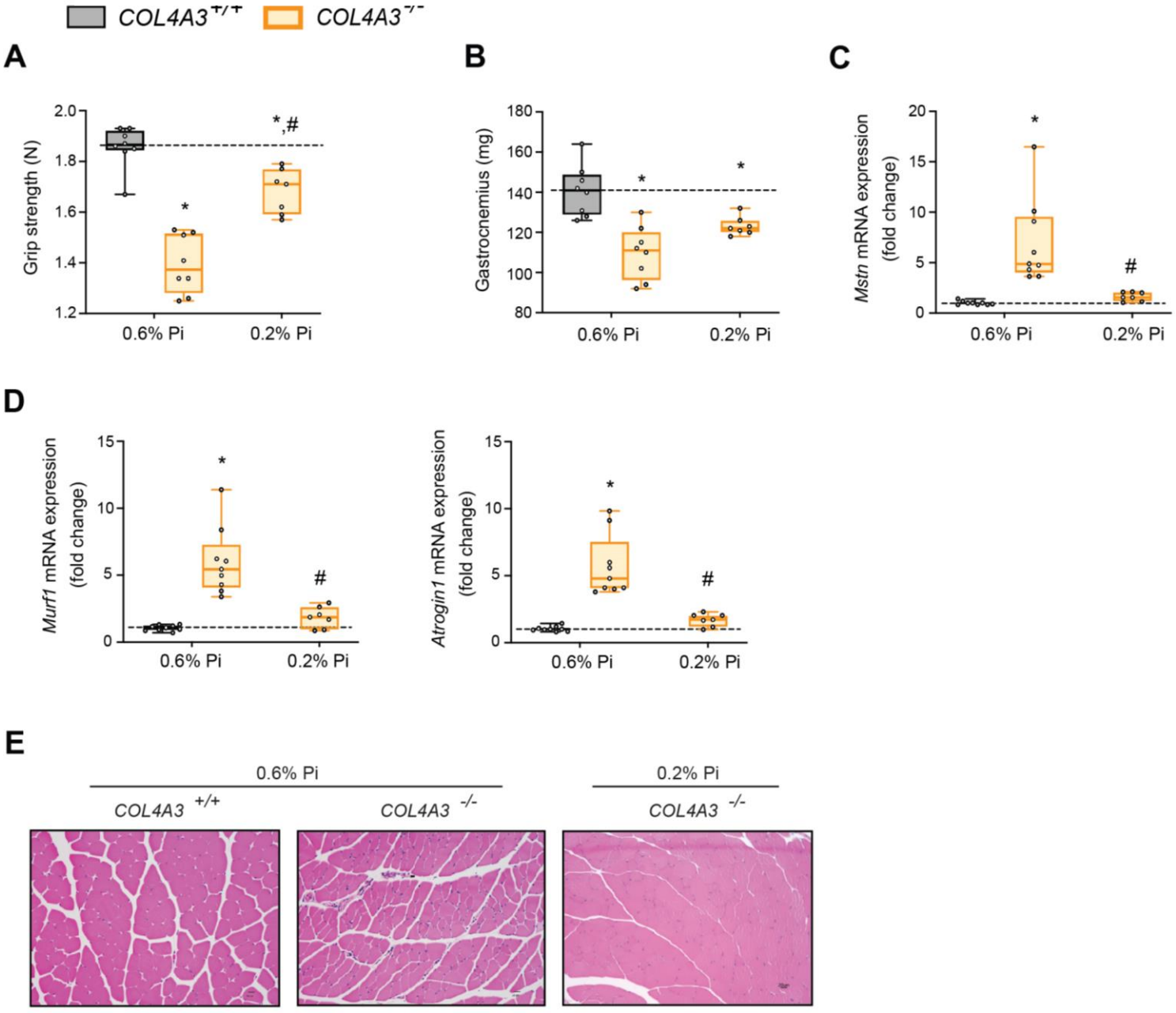

1187

1188

1189

1190

Figure 5. Low Pi feeding counteracts signs of skeletal muscle wasting in *COL4A3*$^{-/-}$ (Alport syndrome) mice.

(**A**) Grip strength. (**B**) Gastrocnemius weight. (**C-D**) qPCR analysis of *Mstn* (C), *Murf1* and *Atrogin1* (D) expression levels in gastrocnemius tissue. (**E**) Representative gross pathology of H&E-stained gastrocnemius sections (scale bar, 20 μm). All values are mean ± SEM (n = 7-9 mice/group; *p ≤ 0.05 vs. COL4A3$^{+/+}$ + 0.6% Pi diet, #p ≤ 0.05 vs. COL4A3$^{-/-}$ + 0.6% Pi diet) where statistical analyses were calculated by two-way ANOVA followed by Tukey's multiple comparison post-hoc test. Dotted lines indicate median *COL4A3*$^{+/+}$ + 0.6% Pi diet measurements.

1201 **Figure 6**

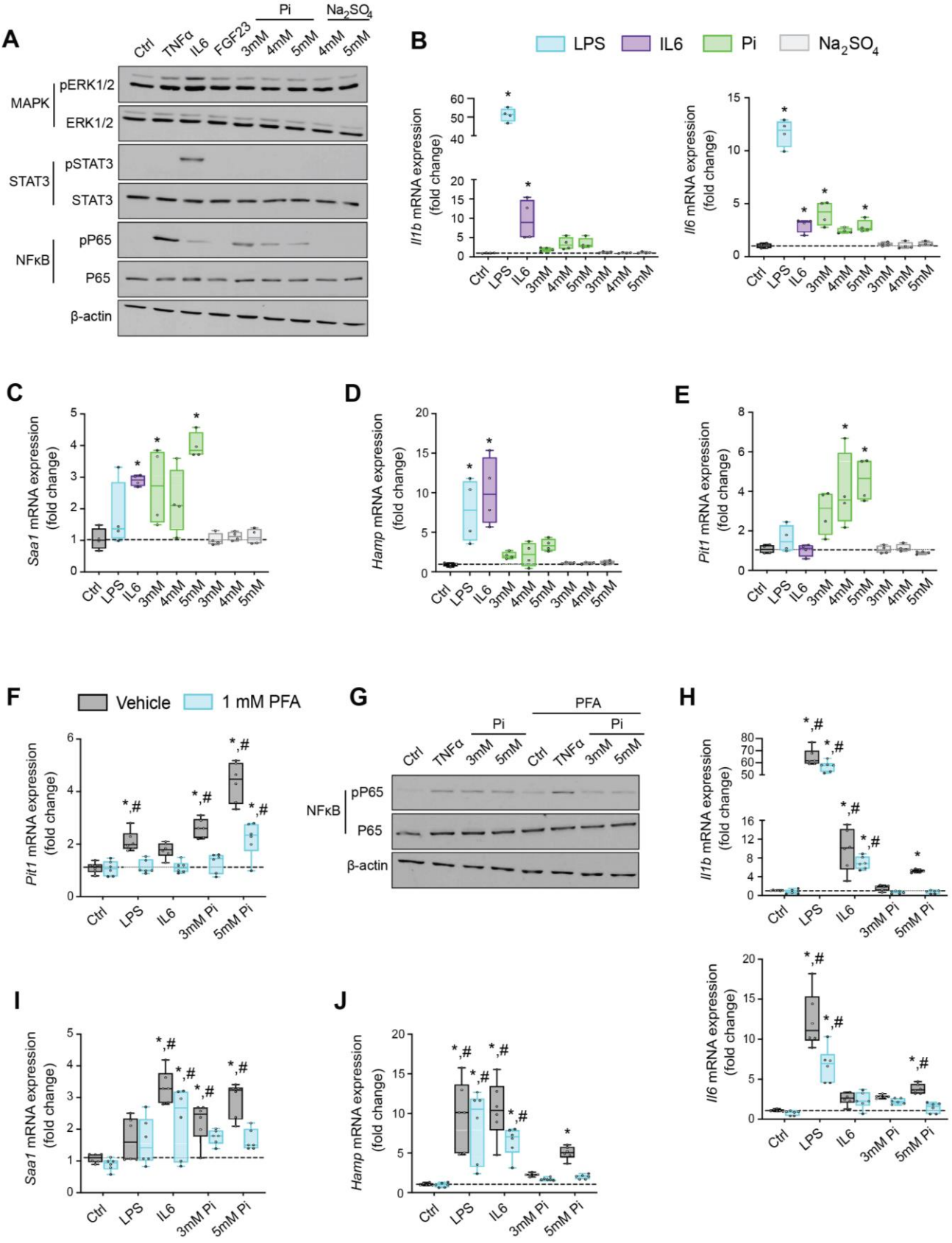

Figure 6. Pi targets hepatocytes and increases expression of inflammatory cytokines and hepcidin.

(**A**) Immunoblot analysis of total protein extracts from primary hepatocytes (n = 5 independent isolations). β-actin serves as loading control. (**B-E**) qPCR analysis of *Il1b*, *Il6*, *Saa1* (B-C), *Hamp* (D) and *Pit1* (E) expression levels in primary hepatocytes; values are mean ± SEM (n = 4 independent isolations; *p ≤ 0.05 vs. control (Ctrl)). Dotted lines indicate median Ctrl measurements. (**F**) qPCR analysis of *Pit1* expression levels in primary hepatocytes following stimuli, with or without phosphonoformic acid (PFA); values are mean ± SEM (n = 6 independent isolations; *p ≤ 0.05 vs. vehicle control (Ctrl), #p ≤ 0.05 vs. 1 mM PFA Ctrl). Dotted lines indicate median vehicle Ctrl measurements. (**G**) Immunoblot analysis of total and phosphorylated p65 (NFκB) protein levels from primary hepatocytes following stimuli, with or without PFA; (n = 5 independent isolations). β-actin serves as loading control. (**H-J**) qPCR analysis of *Il1b*, *Il6*, *Saa1* (H-I) and *Hamp* (J) expression levels in primary hepatocytes following stimuli, with or without PFA; values are mean ± SEM (n = 6 independent isolations; *p ≤ 0.05 vs. vehicle control (Ctrl), #p ≤ 0.05 vs. 1 mM PFA Ctrl) where statistical analyses were calculated by one-way ANOVA (B-E) or by two-way ANOVA (F, H-J) followed by Tukey's multiple comparison post-hoc test. Dotted lines indicate median vehicle Ctrl measurements.

1223 **Figure 7**

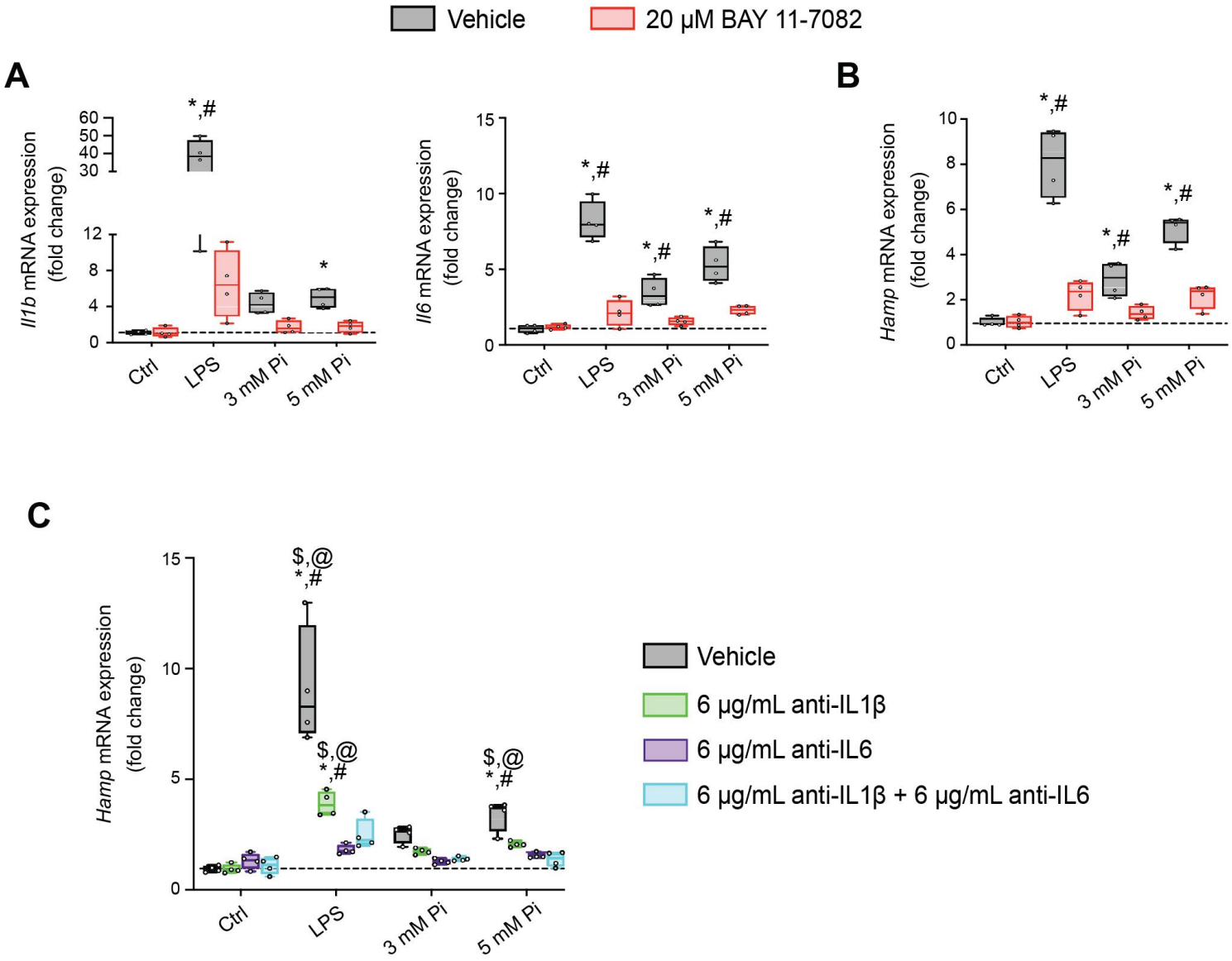

1224

1225

1226

1227

1228

1229

Figure 7. Pi induces hepcidin expression via paracrine IL1β and IL6 signaling

(**A-B**) qPCR analysis of *Il1b*, *Il6* (A) and *Hamp* (B) expression levels in primary hepatocytes following stimuli, with or without BAY 11-7082; values are mean ± SEM (n = 4 independent isolations; *p ≤ 0.05 vs. vehicle control (Ctrl), #p ≤ 0.05 vs. 20 μM BAY 11-7082 Ctrl). Dotted lines indicate median vehicle Ctrl measurements. (**C**) qPCR analysis of *Hamp* expression levels in primary hepatocytes following stimuli with or without anti-IL1β, anti-IL6 or both antibodies in combination; values are mean ± SEM (n = 4 independent isolations; *p ≤ 0.05 vs. vehicle control (Ctrl), #p ≤ 0.05 vs. anti-IL1β Ctrl, $p ≤ 0.05 vs. anti-IL6 Ctrl, @p ≤ 0.05 vs. anti-IL1β + anti-IL6 Ctrl) where statistical analyses were calculated by two-way ANOVA followed by Tukey's multiple comparison post-hoc test. Dotted lines indicate median vehicle Ctrl measurements.

Table 1. Macroscopic parameters of *FGFR4*$^{+/+}$ and *FGFR4*$^{-/-}$ mice receiving control and adenine diet.

	FGFR4$^{+/+}$ + control diet	FGFR4$^{-/-}$ + control diet	FGFR4$^{+/+}$ + adenine diet	FGFR4$^{-/-}$ + adenine diet
Body weight (g)	30.1 ± 0.9	30.2 ± 0.3	16.8*$^{\#}$ ± 0.5	17.5*$^{\#}$ ± 0.4
Liver weight (g)	1.14 ± 0.05	1.22 ± 0.08	0.74*$^{\#}$ ± 0.03	0.78*$^{\#}$ ± 0.05
Spleen weight (mg)	75.0 ± 2.2	76.0 ± 1.7	53.3*$^{\#}$ ± 3.3	56.0*$^{\#}$ ± 3.2
Left kidney weight (mg)	181.8 ± 8.5	173.2 ± 8.3	122.2*$^{\#}$ ± 4.9	101.8*$^{\#}$ ± 7.2
Right kidney weight (mg)	184.7 ± 10.7	175.2 ± 8.2	124.2*$^{\#}$ ± 4.1	102.8*$^{\#}$ ± 7.7

Values are expressed as mean ± SEM. Comparison between groups was performed in form of a two-way ANOVA followed by a post-hoc Tukey test. A level of $P<0.05$ was accepted as statistically significant; N=9/group; *$p \leq 0.05$ vs. FGFR4$^{+/+}$ + control diet, #$p \leq 0.05$ vs. FGFR4$^{-/-}$ + control diet.

Table 2. Macroscopic parameters of *FGFR4*$^{+/+}$ and *FGFR4*$^{-/-}$ mice receiving a graded dietary Pi load.

	FGFR4$^{+/+}$ + 0.7% Pi diet	FGFR4$^{-/-}$ + 0.7% Pi diet	FGFR4$^{+/+}$ + 2% Pi diet	FGFR4$^{-/-}$ + 2% Pi diet	FGFR4$^{+/+}$ + 3% Pi diet	FGFR4$^{-/-}$ + 3% Pi diet
Body weight (g)	32.0 ± 1.0	31.9 ± 1.0	30.3 ± 0.9	31.6 ± 0.9	29.5 ± 0.3	29.5 ± 0.4
Liver weight (g)	1.17 ± 0.04	1.15 ± 0.05	1.24 ± 0.03	1.20 ± 0.05	1.23 ± 0.5	1.19 ± 0.4
Spleen weight (mg)	76.3 ± 2.4	68.3 ± 1.7	77.0 ± 2.8	76.6 ± 2.8	76.6 ± 2.1	74.0 ± 1.7
Left kidney weight (mg)	146.5 ± 4.7	143.6 ± 4.5	156.0 ± 2.9	152.6 ± 3.4	153.4 ± 4.1	152.9 ± 3.7
Right kidney weight (mg)	149.0 ± 3.8	151.5 ± 3.7	152.9 ± 3.2	145.6 ± 3.5	152.5 ± 2.5	149.6 ± 3.9

Values are expressed as mean ± SEM. Comparison between groups was performed in form of a two-way ANOVA followed by a post-hoc Tukey test. No level of statistical significance was accepted between groups; N=8/group

Table 3. Macroscopic parameters of Alport mice receiving either a 0.6% Pi diet or 0.2% Pi diet.

	$COL4A3^{+/+}$ + 0.6% Pi diet	$COL4A3^{-/-}$ + 0.6% Pi diet	$COL4A3^{-/-}$ + 0.2% Pi diet
Body weight (g)	26.3 ± 0.6	16.3* ± 0.6	22.2*$^{\#}$ ± 0.6
Liver weight (g)	1.03 ± 0.04	0.68* ± 0.03	0.90$^{\#}$ ± 0.03
Spleen weight (mg)	72.2 ± 2.3	56.6* ± 2.4	65.9 ± 2.1
Left kidney weight (mg)	145.3 ± 1.6	124.1* ± 2.6	130.1* ± 2.1
Right kidney weight (mg)	147.4 ± 1.6	123.0* ± 3.4	133.6* ± 3.1

Values are expressed as mean ± SEM. Comparison between groups was performed in form of a two-way ANOVA followed by a post-hoc Tukey test. A level of $P<0.05$ was accepted as statistically significant; N=7-9/group; *$p \leq 0.05$ vs. $COL4A3^{+/+}$ + 0.6% Pi diet, #$p \leq 0.05$ vs. $COL4A3^{-/-}$ + 0.6% Pi diet.

Diet	Adenine (g/kg)	Available Pi (%)	Total Ca (%)	Protein source	Energy source	Pi source
TD.170303 (control diet)	0	0.9	0.6	Casein	20% protein 66.9% Carbs 13.2% Fat	Casein Ca Pi, dibasic Na Pi, dibasic
TD.170304 (0.15% adenine)	1.5	0.9	0.6	Casein	20% protein 66.8% Carbs 13.2% Fat	Casein Ca Pi, dibasic Na Pi, dibasic
TD.140290 (0.2% adenine)	2	0.9	0.6	Casein	20% protein 66.8% Carbs 13.2% Fat	Casein Ca Pi, dibasic Na Pi, dibasic

Table 4. Composition of control and adenine diets.

Pi, phosphate; Ca, calcium; Na, sodium. These diets were manufactured by Envigo.

Diet	Available Pi (%)	Total Ca (%)	Total iron (ppm)	Total K (%)	Total Na (%)	Protein source	Energy source	Pi source
TD.180287 (0.7% Pi diet)	0.7	1.9	280	2.4	1.2	Crude	33.3% protein 53.9% Carbs 12.8% Fat	Crude protein
TD.08020 (2% Pi diet)	2.0	1.9	280	1.8	0.9	Crude	33.3% protein 53.9% Carbs 12.8% Fat	Crude protein K Pi, monobasic Na Pi, monobasic
TD.180286 (3% Pi diet)	3.0	1.9	280	2.4	1.2	Crude	33.3% protein 53.9% Carbs 12.8% Fat	Crude protein K Pi, monobasic Na Pi, monobasic

Table 5. Composition of 0.7%, 2% and 3% phosphate (Pi) diets.

Pi, phosphate; Ca, calcium; K, potassium; Na, sodium. These diets were manufactured by Envigo.

Diet	Available Pi (%)	Total Ca (%)	Total iron (ppm)	Total K (%)	Total Na (%)	Protein source	Energy source	Pi source
TD.200407 (0.6% Pi diet, normal)	0.6	0.6	40	0.6	0.38	Egg white solids	17.7% protein 65% Carbs 17.3% Fat	Egg white solids Ca Pi, monobasic
TD.200406 (0.2% Pi diet)	0.2	0.6	40	0.6	0.38	Egg white solids	17.5% protein 65.4% Carbs 17.1% Fat	Egg white solids Ca Pi, monobasic

Table 6. Composition of 0.6% and 0.2% phosphate (Pi) diets.

Pi, phosphate; Ca, calcium; K, potassium; Na, sodium. These diets were manufactured by Envigo.

1342

1343

1344

1345

1346

1347

1348 **Table 7. Oligonucleotides used as sequence specific primers in qPCR analyses**

1349

Gene	Species	Orientation	Primer Sequence (5' – 3')
Npt1/Slc17a1	Mus musculus	Forward Reverse	GGC ACC TCC CTT AGA ACG AG CAG AAC ACA CCC AAC AAT ACC AAA
Npt4/Slc17a3	Mus musculus	Forward Reverse	TGG TAC CCA TTG TTG CTG GC GGG ACA GCT TCA CAA ACG AGT
NaPi2a/Slc34a1	Mus musculus	Forward Reverse	TCA TTG TCA GCA TGG TCT CCT C CCT GCA AAA GCC CGC CTG
NaPi2b/Slc34a2	Mus musculus	Forward Reverse	CTC CTG CTG TCC CTT ACC TG TGT CAT TTG TTT TGC TGG CCT C
NaPi2c/Slc34a3	Mus musculus	Forward Reverse	GAT GCC TTT GAC CTG GTG GA GCC ATG CCA ACC TCT TTC AG
Pit1/Slc20a1	Mus musculus	Forward Reverse	TTC CTT GTT CGT GCG TTC ATC AAT TGG TAA AGC TCG TAA GCC ATT
Pit2/Slc20a2	Mus musculus	Forward Reverse	GAC CGT GGA AAC GCT AAT GG CTC AGG AAG GAC GCG ATC AA
Fgfr1	Mus musculus	Forward Reverse	GCT TGA CGT CGT GGA ACG AT AGC CAC TGA ATG TGA GGC TG
Fgfr2	Mus musculus	Forward Reverse	ATC CCC CTG CGG AGA CA GAG GAC AGA CGC GTT GTT ATC C
Fgfr3	Mus musculus	Forward Reverse	GTG TGC GTG TAA CAG ATG CTC CGG GCG AGT CCA ATA AGG AG
Fgfr4	Mus musculus	Forward Reverse	TGA AGA GTA CCT TGA CCT CCG TCA TGT CGT CTG CGA GTC AG
Alt1/Gpt1	Mus musculus	Forward Reverse	GCC CTC GAG TAC TAT GCG TC TGT CTT GGT ATA CCT CAT CAG CC

Ast1/Got1	Mus musculus	Forward Reverse	CTG AAT GAT CTG GAG AAT GCC C TGC AAA GCC CTG ATA GGC TG
Il6	Mus musculus	Forward Reverse	CTC TGG GAA ATC GTG GAA AT CCA GTT TGG TAG CAT CCA TC
Il1b	Mus musculus	Forward Reverse	TGC CAC CTT TTG ACA GTG ATG TGA TGT GCT GCT GCG AGA TT
Saa1	Mus musculus	Forward Reverse	ACA CCA GCA GGA TGA AGC TAC T GAG CAT GGA AGT ATT TGT CTG AGT
Hamp	Mus musculus	Forward Reverse	GAG CAG CAC CAC CTA TCT CC TTG GTA TCG CAA TGT CTG CC
Haptoglobin/Hp	Mus musculus	Forward Reverse	AGA GAG GCA AGA GAG GTC CA GGC AGC TGT CAT CTT CAA AGT
Atrogin1/Fbxo32	Mus musculus	Forward Reverse	TGA GCG ACC TCA GCA GTT AC GCG CTC CTT CGT ACT TCC TT
Murf1/Trim63	Mus musculus	Forward Reverse	GAG GGC CAT TGA CTT TGG GA TGG TGT TCT TCT TTA CCC TCT GT
Mstn	Mus musculus	Forward Reverse	CTC CAG AAT AGA AGC CAT A GCA GAA GTT GTC TTA TAG C
Mt1	Mus musculus	Forward Reverse	CGA CTT CAA CGT CCT GAG TAC AGG AGC TGG TGC AAG TG
18S rRNA/Rn18s	Mus musculus	Forward Reverse	TTG ACG GAA GGG CAC CAC CAG GCA CCA CCA CCC ACG GAA TCG
Gapdh	Mus musculus	Forward Reverse	CCA ATG TGT CCG TCG TGG ATC T GTT GAA GTC GCA GGA GAC AAC C

1350
1351

Supplementary Figures and Legends

Supplementary Figure 1

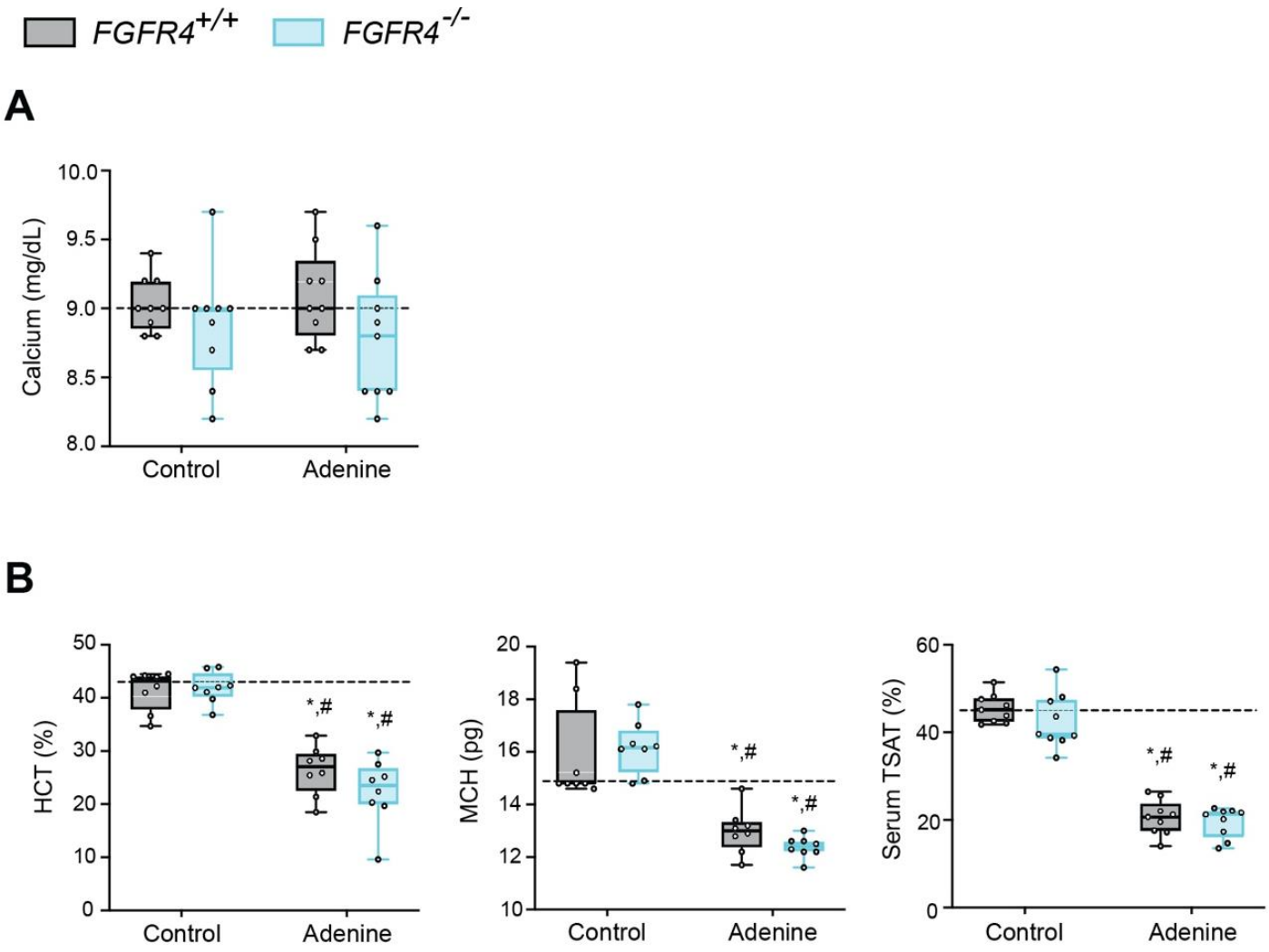

Supplementary Figure 1. FGF23-FGFR4 signaling does not contribute to functional iron deficiency in adenine-induced CKD.

(**A**) Serum calcium analysis from *FGFR4*$^{+/+}$ and *FGFR4*$^{-/-}$ mice, fed either control or adenine diet. (**B**) Hematocrit percentage (HCT%), mean corpuscular hematocrit (MCH) and serum

transferrin saturation percentage (TSAT%) analysis in *FGFR4*$^{+/+}$ and *FGFR4*$^{-/-}$ mice, fed either control or adenine diet. All values are mean ± SEM (n = 8–9 mice/group; *$p \leq 0.05$ vs. FGFR4$^{+/+}$ + control diet, #$p \leq 0.05$ vs. FGFR4$^{-/-}$ + control diet) where statistical analyses were calculated by two-way ANOVA followed by Tukey's multiple comparison post-hoc test. Dotted lines indicate corresponding median measurements from *FGFR4*$^{+/+}$ mice on control diet.

Supplementary Figure 2

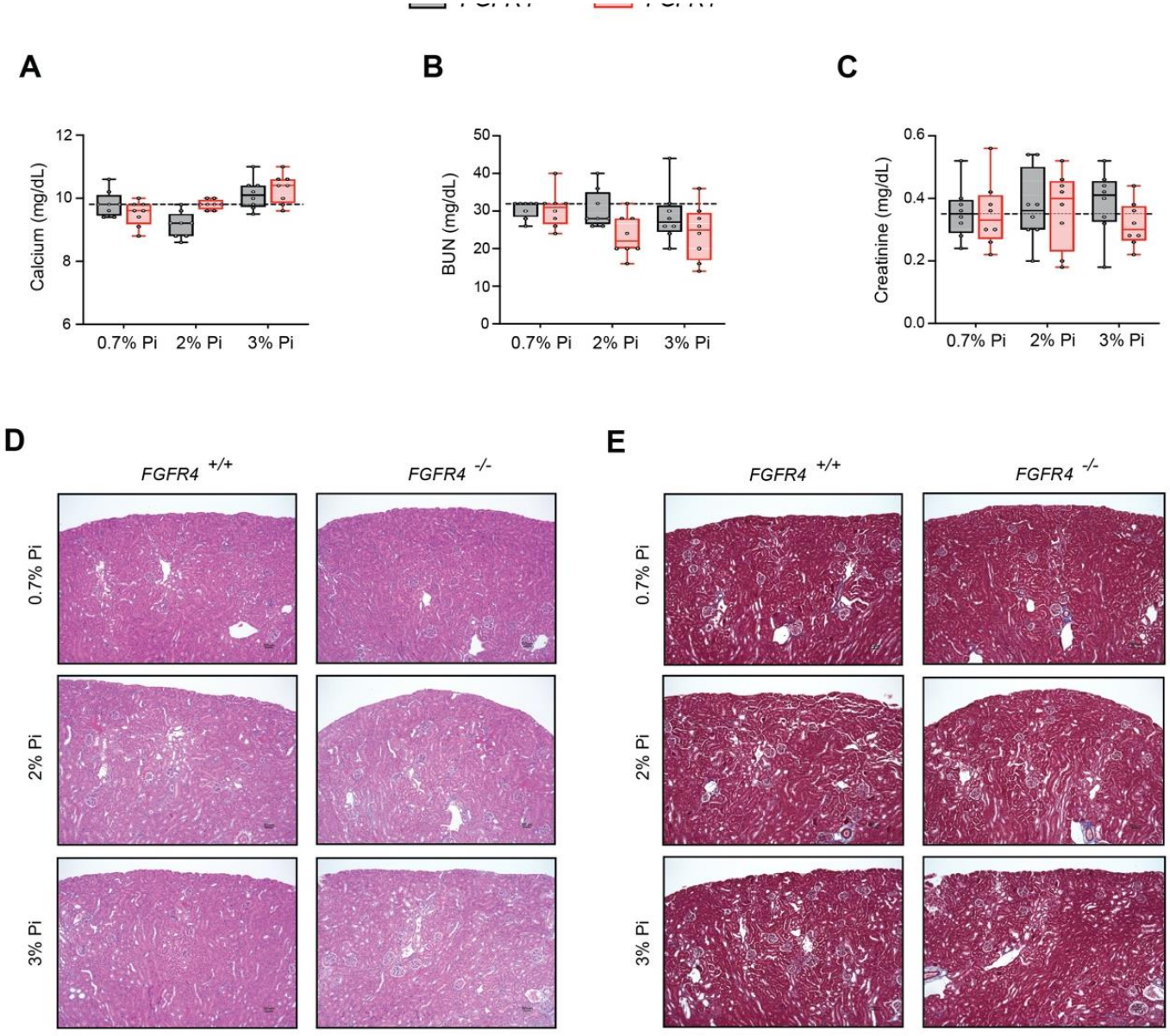

Supplementary Figure 2. FGF23-FGFR4 signaling does not contribute to hypoferremia following dietary Pi overload.

(**A**) Serum calcium analysis from *FGFR4*$^{+/+}$ and *FGFR4*$^{-/-}$ mice, fed either a 0.7% Pi diet or an escalating Pi diet (2% Pi diet or 3% Pi diet). (**B-C**) BUN and serum creatinine analysis from *FGFR4*$^{+/+}$ and *FGFR4*$^{-/-}$ mice, fed either a 0.7% Pi diet or an escalating Pi diet (2% Pi diet or 3%

Pi diet). (**D**) Representative gross pathology of H&E-stained kidney sections (original magnification, 20x; scale bar, 50 μm) from *FGFR4*$^{+/+}$ and *FGFR4*$^{-/-}$ mice, fed either a 0.7% Pi diet or an escalating Pi diet (2% Pi diet or 3% Pi diet). No pathologic changes were detected in sections stained with H&E, as *FGFR4*$^{+/+}$ and *FGFR4*$^{-/-}$ mice on a 2% Pi or 3% Pi diet display similar results to *FGFR4*$^{+/+}$ mice fed a 0.7% Pi diet. (**E**) Representative gross pathology of Masson's trichrome-stained kidney sections (original magnification, 20x; scale bar, 50 μm) from *FGFR4*$^{+/+}$ and *FGFR4*$^{-/-}$ mice, fed either a 0.7% Pi diet or an escalating Pi diet (2% Pi diet or 3% Pi diet). No interstitial fibrosis was detected in sections stained with Masson's trichrome, as *FGFR4*$^{+/+}$ and *FGFR4*$^{-/-}$ mice on a 2% Pi or 3% Pi diet display similar results to *FGFR4*$^{+/+}$ mice fed a 0.7% Pi diet. All values are mean ± SEM (n = 8 mice/group). Dotted lines indicate corresponding median measurements from *FGFR4*$^{+/+}$ mice on 0.7% Pi diet.

Supplementary Figure 3

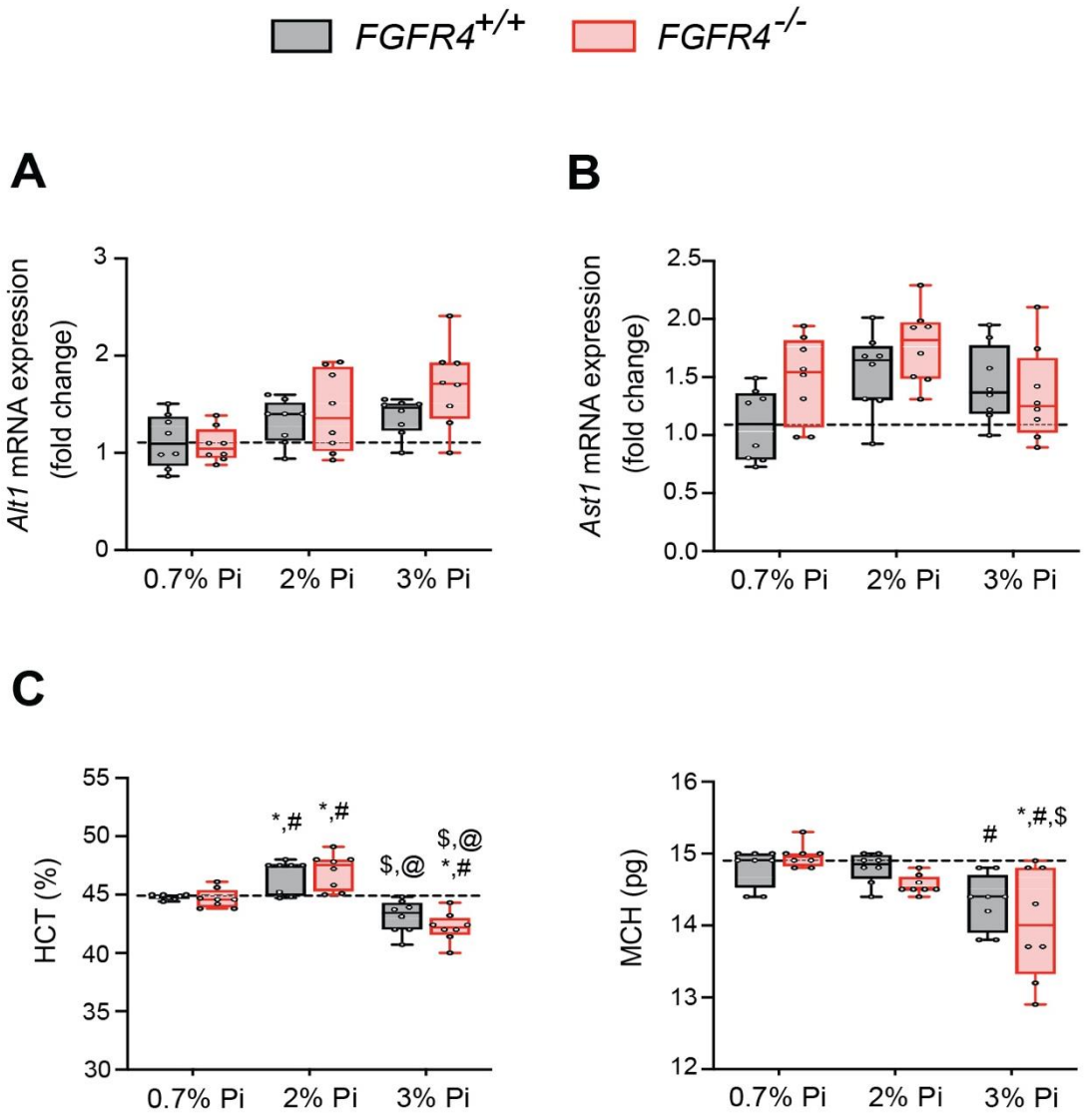

Supplementary Figure 3. Liver injury marker and hematological analyses in *FGFR4*$^{+/+}$ and *FGFR4*$^{-/-}$ mice fed a graded Pi diet.

(**A-B**) qPCR analysis of liver tissue shows expression levels of alanine aminotransferase (*Alt1*) and aspartate aminotransferase (*Ast1*) are not significantly elevated in *FGFR4*$^{+/+}$ and *FGFR4*$^{-/-}$ mice, fed either a 2% Pi diet or 3% Pi diet, when compared to *FGFR4*$^{+/+}$ mice on a 0.7% Pi diet. (**C**) Hematocrit percentage (HCT%) and mean corpuscular hematocrit (MCH) analysis in *FGFR4*$^{+/+}$ and *FGFR4*$^{-/-}$ mice, fed either a 0.7% Pi diet or an escalating Pi diet (2% Pi diet or 3%

Pi diet). All values are mean ± SEM (n = 8 mice/group; *p ≤ 0.05 vs. $FGFR4^{+/+}$ + 0.7% Pi diet, #p ≤ 0.05 vs. $FGFR4^{-/-}$ + 0.7% Pi diet, #p ≤ 0.05 vs. $FGFR4^{+/+}$ + 2% Pi diet, @p ≤ 0.05 vs. $FGFR4^{-/-}$ + 2% Pi diet) where statistical analyses were calculated by two-way ANOVA followed by Tukey's multiple comparison post-hoc test. Dotted lines indicate corresponding median measurements from *$FGFR4^{+/+}$* mice on 0.7% Pi diet.

Supplementary Figure 4

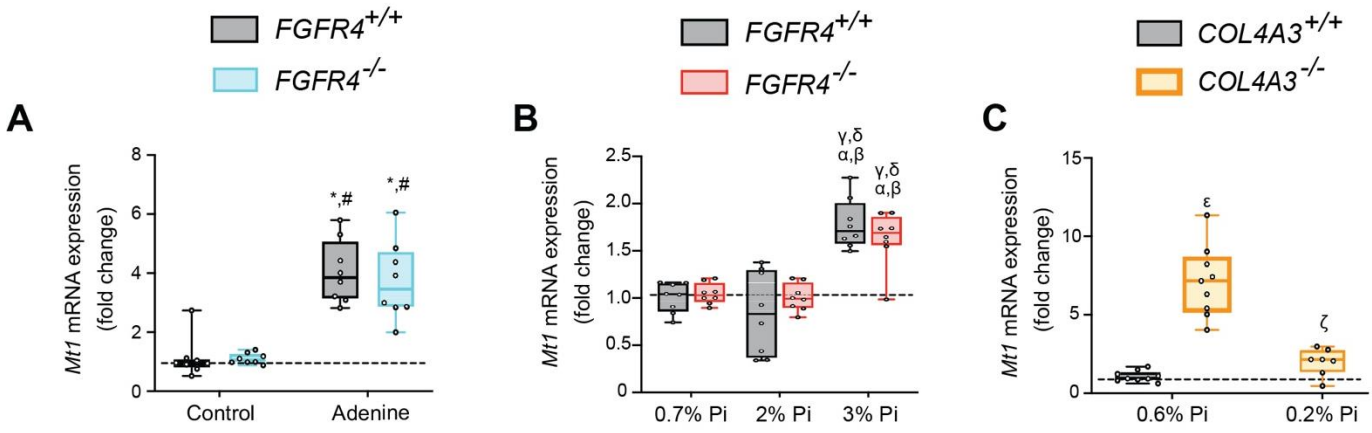

Supplementary Figure 4. Models of hyperphosphatemia exhibit signs of skeletal muscle wasting and low Pi feeding in *COL4A3*$^{-/-}$ (Alport syndrome) mice counteracts muscle dysfunction.

(**A-C**) qPCR analysis of gastrocnemius tissue shows expression levels of metallothionein-1 (*Mt1*) are significantly elevated in *FGFR4*$^{+/+}$ and *FGFR4*$^{-/-}$ mice fed either adenine (A) or a 3% Pi diet (B). Alport (*COL4A3*$^{-/-}$) mice on control diet (0.6% Pi diet) display elevated expression levels of *Mt1* in gastrocnemius tissue, when compared to wild-type (*COL4A3*$^{+/+}$) on a 0.6% Pi diet (C). A low Pi diet (0.2% Pi) in Alport mice reduces *Mt1* expression levels (C). All values are mean ± SEM ((n = 8–9 mice/group; *$p \leq 0.05$ vs. FGFR4$^{+/+}$ + control diet, #$p \leq 0.05$ vs. FGFR4$^{-/-}$ + control diet); (n = 8 mice/group; $^{\alpha}p \leq 0.05$ vs. FGFR4$^{+/+}$ + 0.7% Pi diet, $^{\beta}p \leq 0.05$ vs. FGFR4$^{-/-}$ + 0.7% Pi diet, $^{\gamma}p \leq 0.05$ vs. FGFR4$^{+/+}$ + 2% Pi diet, $^{\delta}p \leq 0.05$ vs. FGFR4$^{-/-}$ + 2% Pi diet); (n = 7-9 mice/group; $^{\varepsilon}p \leq 0.05$ vs. COL4A3$^{+/+}$ + 0.6% Pi diet, $^{\varsigma}p \leq 0.05$ vs. COL4A3$^{-/-}$ + 0.6% Pi diet)) where statistical analyses were calculated by two-way ANOVA followed by Tukey's multiple comparison post-hoc test. Dotted lines indicate corresponding median measurements

from *FGFR4*$^{+/+}$ mice on control diet (A), *FGFR4*$^{+/+}$ mice on 0.7% Pi diet (B) or *COL4A3*$^{+/+}$ mice on 0.6% Pi diet (C).

Supplementary Figure 5

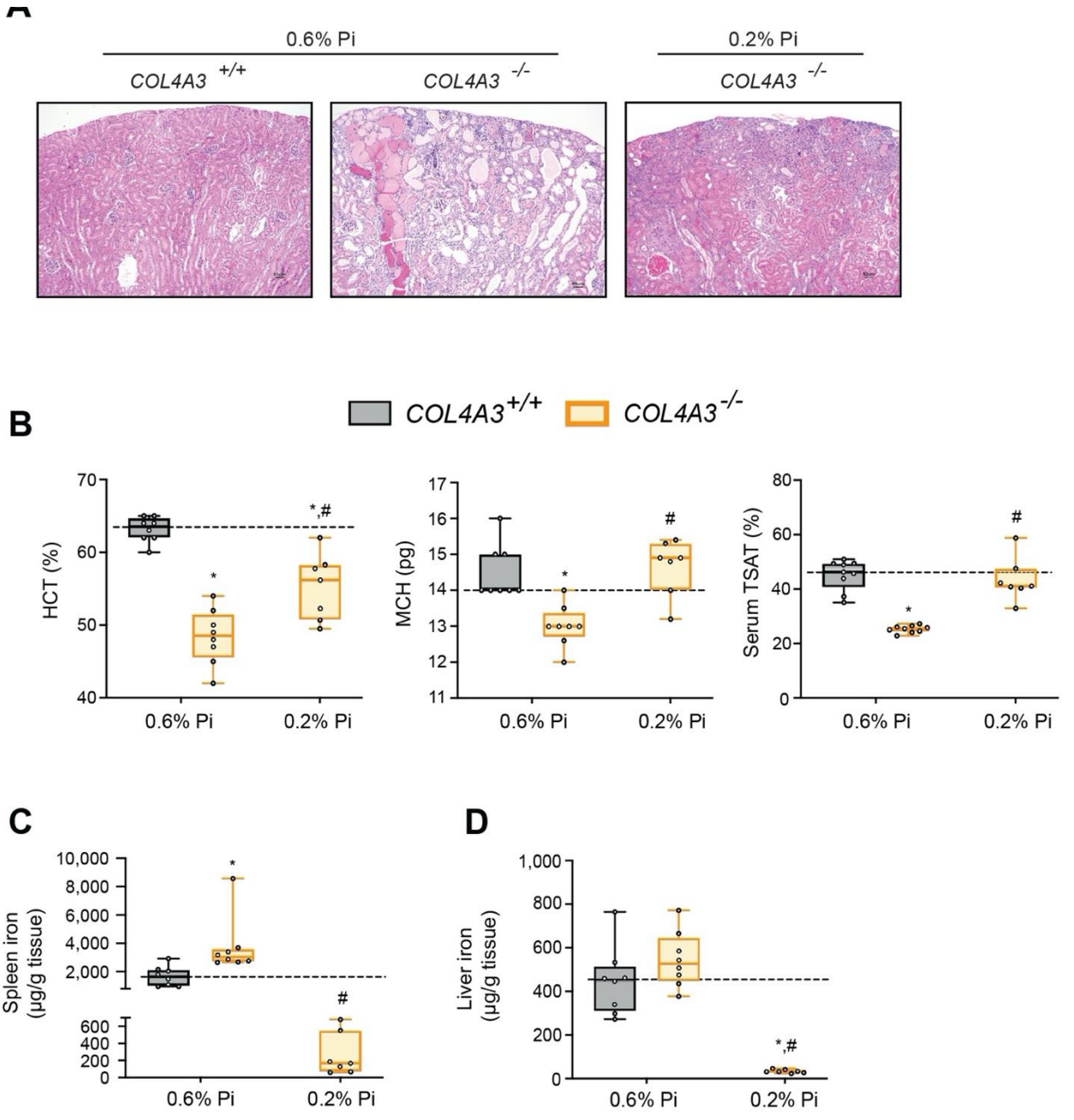

Supplementary Figure 5. Low Pi feeding limits functional iron deficiency in *COL4A3*$^{-/-}$ (Alport syndrome) mice.

(**A**) Representative gross pathology of H&E-stained kidney sections (original magnification, 20x; scale bar, 50 μm) from wild-type (*COL4A3*$^{+/+}$) and Alport (*COL4A3*$^{-/-}$) mice, fed either control diet (0.6% Pi) or a low Pi diet (0.2% Pi). Pathologic changes were detected in sections stained with H&E from Alport mice fed a 0.6% Pi diet. A 0.2% Pi diet moderately improves this feature in Alport mice. (**B**) Hematocrit percentage (HCT%), mean corpuscular hematocrit (MCH) and serum transferrin saturation percentage (TSAT%) analysis in wild-type (*COL4A3*$^{+/+}$) and Alport (*COL4A3*$^{-/-}$) mice, fed either control diet (0.6% Pi) or a low Pi diet (0.2% Pi). (**C**) Spleen non-heme iron concentrations in wild-type (*COL4A3*$^{+/+}$) and Alport (*COL4A3*$^{-/-}$) mice, fed either control diet (0.6% Pi) or a low Pi diet (0.2% Pi). (**D**) Liver non-heme iron concentrations in wild-type (*COL4A3*$^{+/+}$) and Alport (*COL4A3*$^{-/-}$) mice, fed either control diet (0.6% Pi) or a low Pi diet (0.2% Pi). All values are mean ± SEM (n = 7-9 mice/group; *$p \leq 0.05$ vs. COL4A3$^{+/+}$ + 0.6% Pi diet, #$p \leq 0.05$ vs. COL4A3$^{-/-}$ + 0.6% Pi diet) where statistical analyses were calculated by two-way ANOVA followed by Tukey's multiple comparison post-hoc test. Dotted lines indicate corresponding median measurements from *COL4A3*$^{+/+}$ mice on 0.6% Pi diet.

Supplementary Figure 6

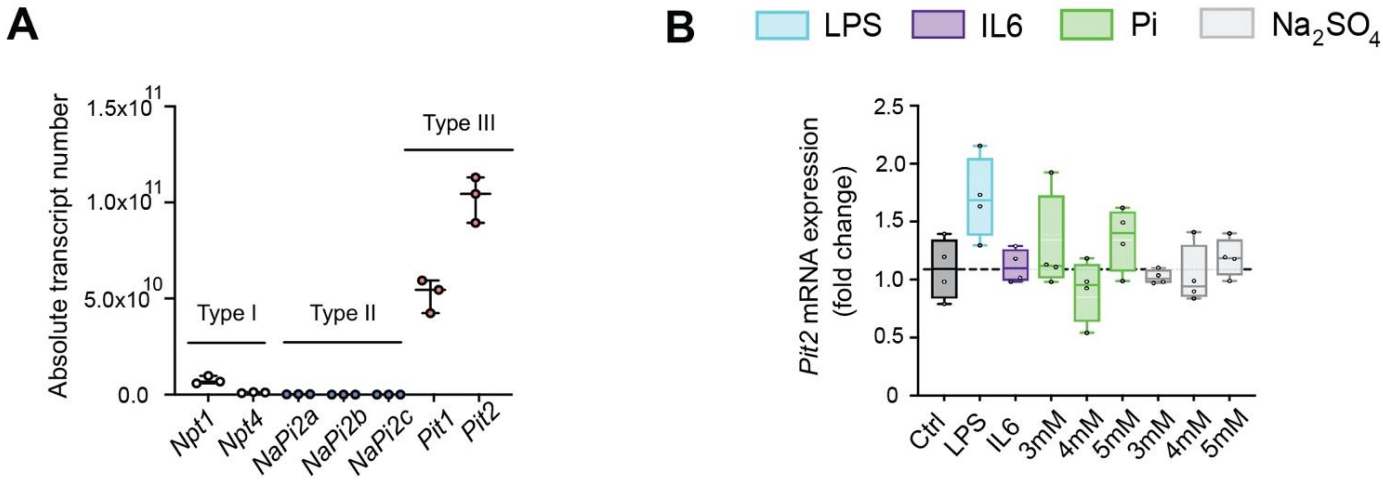

Supplementary Figure 6. Pi targets hepatocytes and increases expression of inflammatory cytokines and hepcidin.

(A) qPCR analysis of isolated primary hepatocytes shows absolute transcript expression of all three families of sodium phosphate cotransporters (type I, type II and type III). This analysis indicates type III sodium phosphate cotransporters (*Pit1* and *Pit2*) have the highest expression levels in mouse primary hepatocyte cultures (n = 3 independent isolations). **(B)** qPCR analysis of primary hepatocytes shows *Pit2* expression levels following inflammatory, dose-dependent Pi or dose-dependent Na_2SO_4 treatment. No significant elevations were detected following treatments, when compared to control (Ctrl); values are mean ± SEM (n = 4 independent isolations). Dotted lines indicate corresponding median measurements from Ctrl.

Supplementary Figure 7

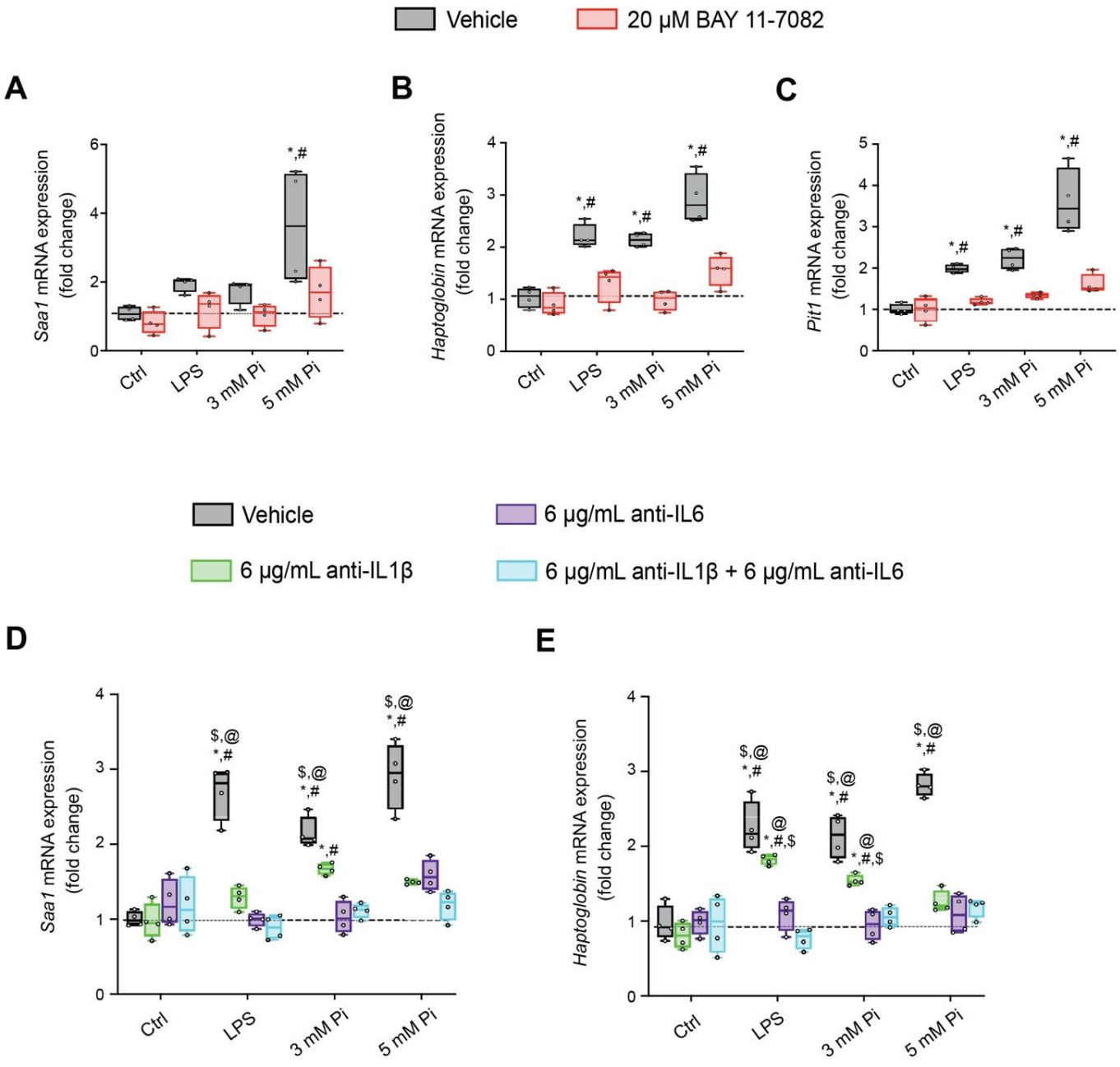

Supplementary Figure 7. Pi induces hepcidin expression via paracrine IL1β and IL6 signaling.

(**A-C**) qPCR analysis of primary hepatocytes shows expression levels of *Saa1* (A), *Haptoglobin* (B) and *Pit1* (B) following lipopolysaccharide (LPS) or Pi stimulation, with or without BAY 11-7082; values are mean ± SEM (n = 4 independent isolations; *p ≤ 0.05 vs. vehicle control (Ctrl), #p ≤ 0.05 vs. 20 μM BAY 11-7082 Ctrl). Dotted lines indicate corresponding median measurements from vehicle Ctrl. (**D-E**) qPCR analysis of primary hepatocytes shows *Saa1* and *Haptoglobin* expression levels following LPS or Pi stimulation, with or without anti-IL1β, anti-IL6 or both antibodies in combination; values are mean ± SEM (n = 4 independent isolations; *p ≤ 0.05 vs. vehicle control (Ctrl), #p ≤ 0.05 vs. anti-IL1β Ctrl, $p ≤ 0.05 vs. anti-IL6 Ctrl, @p ≤ 0.05 vs. anti-IL1β + anti-IL6 Ctrl) where statistical analyses were calculated by two-way ANOVA followed by Tukey's multiple comparison post-hoc test. Dotted lines indicate corresponding median measurements from vehicle Ctrl.